MITP/17-005

A Tale of Two Portals: Testing Light, Hidden New Physics at Future e^+e^- Colliders

Jia Liu,* Xiao-Ping Wang,† and Felix Yu‡

PRISMA Cluster of Excellence & Mainz Institute for Theoretical Physics,

Johannes Gutenberg University, 55099 Mainz, Germany

(Dated: April 5, 2017)

We investigate the prospects for producing new, light, hidden states at a future e^+e^- collider in a Higgsed dark $U(1)_D$ model, which we call the Double Dark Portal model. The simultaneous presence of both vector and scalar portal couplings immediately modifies the Standard Model Higgsstrahlung channel, $e^+e^- \to Zh$, at leading order in each coupling. In addition, each portal leads to complementary signals which can be probed at direct and indirect detection dark matter experiments. After accounting for current constraints from LEP and LHC, we demonstrate that a future e^+e^- Higgs factory will have unique and leading sensitivity to the two portal couplings by studying a host of new production, decay, and radiative return processes. Besides the possibility of exotic Higgs decays, we highlight the importance of direct dark vector and dark scalar production at e^+e^- machines, whose invisible decays can be tagged from the recoil mass method.

* liuj@uni-mainz.de

† xiaowang@uni-mainz.de

‡ yu001@uni-mainz.de

CONTENTS

I. INTRODUCTION

Searches for new, light, hidden states are strongly motivated from the overriding question of determining the particle nature of dark matter. The possible couplings to such light states, however, remain highly model-dependent. Because higher dimension operators are expected to be suppressed in scattering processes at low energies, the most promising couplings give marginal Lagrangian operators at dimension four. Along these lines, two well-studied couplings are a new kinetic mixing term ϵ between a new, light, hidden photon and the hypercharge gauge boson and a new quartic Higgs portal coupling λ_{HP} between a hidden charged scalar field and the Standard Model Higgs field.

In this work, we argue and demonstrate that both marginal couplings can be simultaneously probed in future measurements of a high energy e^+e^- collider. Such a collider is, of course, very strongly motivated by a rich and diverse set of possible Higgs measurements, with leading sensitivity to the total Higgs width, Higgs couplings to Standard Model (SM) particles, exotic Higgs decays, and additional precision measurements of the top quark mass and exotic Z boson decays if additional running conditions are afforded [1–4]. We highlight that such a machine also has leading sensitivity to new, weakly coupled, hidden sectors, which can be probed via both radiative return processes and exotic invisible and semi-visible Higgs decays. We will show that these measurements are enabled because of the expected high precision photon resolution in the electromagnetic calorimeter, the exquisite reconstruction of charged leptons, and clean discrimination of exotic signals from SM background processes.

Both of these marginal operators have been studied autonomously at electron colliders in the hidden photon context [5–15] and the hidden scalar context [16–21]. Some works study both operators in tandem [22–24]. The current status of light, sub-GeV hidden photon searches and future prospects is summarized in Ref. [25]. In contrast with previous studies, we focus on higher

mass hidden photons beyond the reach of B-physics experiments and beam-dump experiments. In addition, we will emphasize the unique capability of e^+e^- machines to reconstruct invisible decays, which is a marked improvement over the reconstruction prospects at hadron colliders.

The lack of evidence for weakly interacting massive particles (WIMPs) in direct detection (DD) experiments [26–29], increasingly strong constraints on thermal WIMPs from indirect detection (ID) experiments [30–34], and non-observation of beyond the Standard Model (BSM) missing transverse energy signatures at the LHC [35, 36], combine to an increasing unease with the standard WIMP miracle paradigm. On the other hand, dark matter coupled to kinetically mixed hidden photons suffers from strong direct detection constraints (see, *e.g.*, [37]). A consistent dark matter model must hence simultaneously address the relic density mechanism and non-observation in the current experimental probes, and thus minimal models either require nonthermal dark matter production in the early universe, coannihilation channels [38–40], or resonant dark matter annihilation in order to divorce the early universe dynamics from collider processes (see, *e.g.*, [41]). Moreover, while the nuclear recoil energy spectrum at direct detection experiments requires the dark matter mass as input, colliders instead probe mediator masses if they are on-shell, which shows the complementarity between both approaches. In our work, we will further demonstrate these complementary aspects between dark matter experiments and hadron and lepton colliders in the context of our dark matter model.

In Sec. II, we review the theoretical framework for the Double Dark Portal model, which unifies the kinetic mixing portal and the scalar Higgs portal into a minimal setup with dark matter. In Sec. III, we detail the phenomenology of the dark matter for direct detection and indirect detection experiments. We discuss the extensive collider phenomenology of the model and review the current constraints from experiments at the Large Electron-Positron (LEP) collider and the Large Hadron Collider (LHC) in Sec. IV. We then present the prospects for exploring new, light hidden states at a future e^+e^- machine in Sec. V and conclude in Sec. VI. In Appendix A, we offer some detailed discussion of limiting cases in our Double Dark Portal model for pedagogical clarity, and we discuss a cancellation effect in scattering processes via kinetic mixing in Appendix B. We also present the dark matter annihilation cross sections for charged SM final states in Appendix C.

II. OVERVIEW OF THE DOUBLE DARK PORTAL MODEL: SIMULTANEOUS KINETIC MIXING AND SCALAR PORTAL COUPLINGS

We begin with the Lagrangian of the Double Dark Portal Model,

$$\begin{aligned}\mathcal{L} \supset & -\tfrac{1}{4}B_{\mu\nu}B^{\mu\nu} - \tfrac{1}{4}W^i_{\mu\nu}W^{i\,\mu\nu} - \tfrac{1}{4}K_{\mu\nu}K^{\mu\nu} + \tfrac{\epsilon}{2\cos\theta_W}B_{\mu\nu}K^{\mu\nu} \\ & + |D_\mu H|^2 + |D_\mu \Phi|^2 + \mu_H^2|H|^2 - \lambda_H|H|^4 + \mu_D^2|\Phi|^2 - \lambda_D|\Phi|^4 - \lambda_{HP}|H|^2|\Phi|^2 \\ & + \bar{\psi}(i\not{D} - m_\psi)\psi \ ,\end{aligned} \tag{1}$$

where $K_{\mu\nu}$ is the field strength tensor for the $U(1)_D$ gauge boson, Φ is a dark Higgs scalar field with charge $+1$ under $U(1)_D$, and ψ is the dark matter and a SM gauge singlet fermion with charge $+1$ under $U(1)_D$. We take $\mu_H^2 > 0$ and $\mu_D^2 > 0$, which trigger spontaneous symmetry breaking of the SM electroweak symmetry and the $U(1)_D$ dark gauge symmetry, respectively. The θ_W parameter is the tree-level SM weak mixing angle, $\theta_W = \tan^{-1}(g'/g)$. The nonzero Higgs portal coupling, λ_{HP}, induces mass mixing between the h and ϕ scalars, which results in mass eigenstates H_0 and S. Simultaneously, the kinetic mixing ϵ will result in an effective mass mixing between the SM Z gauge boson and the K dark gauge boson, which results in the mass eigenstates $\tilde{Z}$ and $\tilde{K}$. The two marginal couplings, ϵ and λ_{HP}, are commonly referred to as vector and scalar portals, respectively [42]. Because the phenomenology of such portal couplings changes significantly when a light dark matter particle is added, we call the Lagrangian in Eq. (1) the Double Dark Portal (DDP) model.

We solve the Lagrangian in the broken phase after the Higgs and the dark Higgs obtain their vacuum expectation values (vevs),

$$\Phi = \frac{1}{\sqrt{2}}(v_D + \phi) \ , \tag{2}$$

$$H = \frac{1}{\sqrt{2}}(v_H + h) \ , \tag{3}$$

by diagonalizing and canonically normalizing the kinetic terms for the electrically neutral gauge bosons and diagonalizing their mass matrix. We can rewrite the Lagrangian using matrix notation, with mass terms acting on the gauge basis vector $(\ W^3_\mu \ \ B_\mu \ \ K_\mu\ )^T$ as

$$\mathcal{L} \supset \frac{1}{2}\begin{pmatrix} W^{\mu\,3} & B^\mu & K^\mu \end{pmatrix}\begin{pmatrix} g^2\frac{v_H^2}{4} & -g'g\frac{v_H^2}{4} & 0 \\ -g'g\frac{v_H^2}{4} & g'^2\frac{v_H^2}{4} & 0 \\ 0 & 0 & g_D^2 v_D^2 \end{pmatrix}\begin{pmatrix} W^3_\mu \\ B_\mu \\ K_\mu \end{pmatrix} \ . \tag{4}$$

In this breaking of $SU(2)_L \times U(1)_Y \times U(1)_D \to U(1)_{\rm em}$, the resulting field strength tensors of the individual neutral vectors corresponding to the gauge eigenstates W^3, B, and K all have Abelian field strengths, while non-Abelian vector interactions are inherited from the $SU(2)_L$ gauge boson field strength tensor. We will not explicitly write the non-Abelian vector interactions in the following, but instead understand that they are correspondingly modified when we perform the rescaling needed to canonically normalize the Abelian field strengths of the neutral vectors.[1]

A. Neutral vector boson mixing

To simplify the Lagrangian in the broken phase, we first rotate by the tree-level SM weak mixing angle, which reduces the mass matrix to rank 2 and correspondingly modifies the kinetic mixing between the Abelian field strengths. Explicitly, we sandwich $R_{\theta W} R_{\theta W}^T$ twice in Eq. (4), with

$$R_{\theta W} = \begin{pmatrix} c_W & s_W & 0 \\ -s_W & c_W & 0 \\ 0 & 0 & 1 \end{pmatrix} , \tag{5}$$

$c_W = \cos\theta_W$ and $s_W = \sin\theta_W$, which gives

$$\begin{aligned} \mathcal{L} \supset & \frac{-1}{4} \begin{pmatrix} Z_{\rm SM}^{\mu\nu} & A_{\rm SM}^{\mu\nu} & K^{\mu\nu} \end{pmatrix} \begin{pmatrix} 1 & 0 & \epsilon t_W \\ 0 & 1 & -\epsilon \\ \epsilon t_W & -\epsilon & 1 \end{pmatrix} \begin{pmatrix} Z_{\mu\nu,\,\rm SM} \\ A_{\mu\nu,\,\rm SM} \\ K_{\mu\nu} \end{pmatrix} \\ & + \frac{1}{2} \begin{pmatrix} Z_{\rm SM}^{\mu} & A_{\rm SM}^{\mu} & K^{\mu} \end{pmatrix} \begin{pmatrix} m_{Z,\,\rm SM}^2 & 0 & 0 \\ 0 & 0 & 0 \\ 0 & 0 & m_K^2 \end{pmatrix} \begin{pmatrix} Z_{\mu,\,\rm SM} \\ A_{\mu,\,\rm SM} \\ K_{\mu} \end{pmatrix} , \end{aligned} \tag{6}$$

where $t_W = \tan\theta_W$, $m_{Z,\,\rm SM}^2 = (g^2 + g'^2)v_H^2/4$ is the tree-level SM Z-boson mass, and $m_K^2 = g_D^2 v_D^2$ is the tree-level $U(1)_D$ gauge boson mass. To canonically normalize the kinetic terms for the neutral

[1] We remark that the Stueckelberg mechanism [43, 44] provides an alternative mass generation for $\tilde{K}$, which we do not employ here. The collider phenomenology of a dark neutral gauge boson with mass arising from the Stuckelberg mechanism is presented in Ref. [44].

gauge bosons, we use the successive transformations

$$U_1 = \begin{pmatrix} 1 & 0 & 0 \\ -\epsilon^2 t_W & 1 & \epsilon \\ -\epsilon t_W & 0 & 1 \end{pmatrix} , \quad U_2 = \begin{pmatrix} \sqrt{\dfrac{1-\epsilon^2}{1-\epsilon^2 c_W^{-2}}} & 0 & 0 \\ 0 & 1 & 0 \\ \dfrac{-\epsilon^3 t_W}{\sqrt{(1-\epsilon^2)(1-\epsilon^2 c_W^{-2})}} & 0 & \dfrac{1}{\sqrt{1-\epsilon^2}} \end{pmatrix} , \tag{7}$$

which give

$$\begin{aligned} \mathcal{L} \supset & \frac{-1}{4} \begin{pmatrix} Z^{\mu\nu}_{\rm SM} & A^{\mu\nu}_{\rm SM} & K^{\mu\nu} \end{pmatrix} (U_1^T)^{-1}(U_2^T)^{-1}\mathbb{I}_3 U_2^{-1}U_1^{-1} \begin{pmatrix} Z_{\mu\nu,\,\rm SM} \\ A_{\mu\nu,\,\rm SM} \\ K_{\mu\nu} \end{pmatrix} \\ & + \frac{1}{2} \begin{pmatrix} Z^{\mu}_{\rm SM} & A^{\mu}_{\rm SM} & K^{\mu} \end{pmatrix} (U_1^T)^{-1}(U_2^T)^{-1} \begin{pmatrix} \dfrac{m^2_{Z,\,\rm SM}(1-\epsilon^2)^2 + m_K^2\epsilon^2 t_W^2}{(1-\epsilon^2)(1-\epsilon^2 c_W^{-2})} & 0 & \dfrac{-m_K^2\epsilon t_W}{(1-\epsilon^2)\sqrt{1-\epsilon^2 c_W^{-2}}} \\ 0 & 0 & 0 \\ \dfrac{-m_K^2\epsilon t_W}{(1-\epsilon^2)\sqrt{1-\epsilon^2 c_W^{-2}}} & 0 & \dfrac{m_K^2}{1-\epsilon^2} \end{pmatrix} \\ & \times U_2^{-1}U_1^{-1} \begin{pmatrix} Z_{\mu,\,\rm SM} \\ A_{\mu,\,\rm SM} \\ K_{\mu} \end{pmatrix} , \end{aligned} \tag{8}$$

where the kinetic terms are now canonically normalized and only one further unitary rotation is needed to diagonalize the mass matrix. We remark that $|\epsilon| < c_W$ is required to ensure the kinetic mixing matrix in Eq. (6) has a positive definite determinant, which allows U_2 to remain non-singular. The final Jacobi rotation required is

$$R_M = \begin{pmatrix} c_M & 0 & s_M \\ 0 & 1 & 0 \\ -s_M & 0 & c_M \end{pmatrix} \tag{9}$$

for $c_M = \cos\theta_M$ and $s_M = \sin\theta_M$ and θ_M defined by $\tan\theta_M = \dfrac{1}{\beta \pm \sqrt{\beta^2+1}}$ for

$$\beta \equiv \frac{m^2_{Z,\,\rm SM}(1-\epsilon^2)^2 - m_K^2(1-\epsilon^2 c_W^{-2}(1+s_W^2))}{2m_K^2\epsilon t_W\sqrt{1-\epsilon^2 c_W^{-2}}} , \tag{10}$$

and the upper (lower) sign in $\tan\theta_M$ corresponds to $m_{Z,\,\mathrm{SM}} > m_K$ ($m_{Z,\,\mathrm{SM}} < m_K$). The resulting non-zero mass eigenvalues are

$$m^2_{\tilde{K}},\, m^2_{\tilde{Z}} = \frac{m^2_{Z,\,\mathrm{SM}}(1-\epsilon^2) + m^2_K \pm \sqrt{(-m^2_{Z,\,\mathrm{SM}}(1-\epsilon^2)+m^2_K)^2 + 4m^2_{Z,\,\mathrm{SM}} m^2_K \epsilon^2 t^2_W}}{2(1-\epsilon^2 c_W^{-2})}\,, \tag{11}$$

and the corresponding neutral vector basis is $R_M^T U_2^{-1} U_1^{-1} (\; Z_{\mu,\,\mathrm{SM}} \;\; A_{\mu,\,\mathrm{SM}} \;\; K_\mu \;)^T$. We remark that these are exact expressions valid for arbitrary ϵ.

For $\epsilon \ll 1$, we provide compact expressions for the masses and the corresponding gauge fields in the mass basis. To $\mathcal{O}(\epsilon^3)$,

$$m^2_{\tilde{K}} = m^2_K + \frac{m^2_K c_W^{-2}\epsilon^2 (m^2_{Z,\,\mathrm{SM}} c^2_W - m^2_K)}{m^2_{Z,\,\mathrm{SM}} - m^2_K}\,, \quad m^2_{\tilde{Z}} = m^2_{Z,\,\mathrm{SM}} + \frac{m^4_{Z,\,\mathrm{SM}} t^2_W \epsilon^2}{m^2_{Z,\,\mathrm{SM}} - m^2_K} \tag{12}$$

and

$$\begin{pmatrix} \tilde{Z}_\mu \\ \tilde{A}_\mu \\ \tilde{K}_\mu \end{pmatrix} = R_M^T U_2^{-1} U_1^{-1} \begin{pmatrix} Z_{\mu,\,\mathrm{SM}} \\ A_{\mu,\,\mathrm{SM}} \\ K_\mu \end{pmatrix} = \tag{13}$$

$$\begin{pmatrix} Z_{\mu,\,\mathrm{SM}} - \dfrac{t_W m^2_K}{m^2_{Z,\,\mathrm{SM}} - m^2_K}\epsilon K_\mu - \dfrac{m^4_{Z,\,\mathrm{SM}} t^2_W}{2(m^2_{Z,\,\mathrm{SM}} - m^2_K)^2}\epsilon^2 Z_{\mu,\,\mathrm{SM}} \\ A_{\mu,\,\mathrm{SM}} - \epsilon K_\mu \\ K_\mu + \dfrac{t_W m^2_{Z,\,\mathrm{SM}}}{m^2_{Z,\,\mathrm{SM}} - m^2_K}\epsilon Z_{\mu,\,\mathrm{SM}} - \left(\dfrac{1}{2} + \dfrac{m^4_K t^2_W}{2(m^2_{Z,\,\mathrm{SM}} - m^2_K)^2}\right)\epsilon^2 K_\mu \end{pmatrix}. \tag{14}$$

We note that this expansion for $\epsilon \ll 1$ is insufficient for $m_K \to 0$ or $m_K \to m_{Z,\,\mathrm{SM}}$. These two limits are discussed in Appendix A. Given that ϵ is small, the masses of $\tilde{K}$ and $\tilde{Z}$ are altered only at the ϵ^2 level.

With the $\mathcal{O}(\epsilon^3)$ expressions for the mass eigenstate vectors with canonically normalized kinetic terms, we can now write down the corresponding currents associated with the mass eigenstate vectors:

$$\begin{aligned}
\mathcal{L} \supset\; & g Z_{\mu,\,\mathrm{SM}} J^\mu_Z + e A_{\mu,\,\mathrm{SM}} J^\mu_{\mathrm{em}} + g_D K_\mu J^\mu_D \\
&= \tilde{Z}_\mu \left(g J^\mu_Z - g_D \frac{m^2_{Z,\,\mathrm{SM}} t_W}{m^2_{Z,\,\mathrm{SM}} - m^2_K}\epsilon J^\mu_D + g \frac{m^2_{Z,\,\mathrm{SM}}(m^2_{Z,\,\mathrm{SM}} - 2m^2_K) t^2_W}{2(m^2_K - m^2_{Z,\,\mathrm{SM}})^2}\epsilon^2 J^\mu_Z - e \frac{m^2_{Z,\,\mathrm{SM}} t_W}{m^2_{Z,\,\mathrm{SM}} - m^2_K}\epsilon^2 J^\mu_{\mathrm{em}} \right) \\
&\quad + \tilde{K}_\mu \left(g_D J^\mu_D + g \frac{m^2_K t_W}{m^2_{Z,\,\mathrm{SM}} - m^2_K}\epsilon J^\mu_Z + e\epsilon J^\mu_{\mathrm{em}} + g_D \frac{(m^4_{Z,\,\mathrm{SM}} c^2_W - 2m^2_K m^2_{Z,\,\mathrm{SM}} + m^4_K) c_W^{-2}}{2(m^2_{Z,\,\mathrm{SM}} - m^2_K)^2}\epsilon^2 J^\mu_D \right) \\
&\quad + \tilde{A}_\mu e J^\mu_{\mathrm{em}}\,.
\end{aligned} \tag{15}$$

Again, the situation for $m_K \to 0$ or $m_K \to m_{Z,\,\mathrm{SM}}$ is discussed in Appendix A. From these expressions, we see explicitly that SM fermions, encoded via J^μ_{em} and J^μ_Z, obtain an $\mathcal{O}(\epsilon)$ electric charge and an $\mathcal{O}(\epsilon)$ neutral weak charge mediated by $\tilde{K}_\mu$. Matter charged in the $U(1)_D$ sector correspondingly receives an $\mathcal{O}(\epsilon)$ dark charge mediated by $\tilde{Z}_\mu$.

B. Scalar boson mixing

The analysis of the scalar sector is simpler and follows previous discussions of scalar Higgs portals in the literature (see, *e.g.* [45]). From Eq. (2) and Eq. (3), we have

$$\mu_D^2 = \lambda_D v_D^2 + \frac{1}{2}\lambda_{HP} v_H^2 \ , \tag{16}$$

$$\mu_H^2 = \lambda_H v_H^2 + \frac{1}{2}\lambda_{HP} v_D^2 \ . \tag{17}$$

The scalar mass eigenstates are then

$$\begin{pmatrix} S \\ H_0 \end{pmatrix} = \begin{pmatrix} \cos\alpha & \sin\alpha \\ -\sin\alpha & \cos\alpha \end{pmatrix} \begin{pmatrix} \phi \\ h \end{pmatrix} , \tag{18}$$

where

$$\tan 2\alpha = \frac{\lambda_{HP} v_H v_D}{\lambda_D v_D^2 - \lambda_H v_H^2} \tag{19}$$

is the scalar mixing angle. The scalar masses are

$$m^2_{S,\,H_0} = \lambda_H v_H^2 + \lambda_D v_D^2 \pm \sqrt{(\lambda_H v_H^2 - \lambda_D v_D^2)^2 + \lambda_{HP} v_H^2 v_D^2} \ . \tag{20}$$

We can thus reparametrize the scalar Lagrangian couplings μ_D, μ_H, λ_D, λ_H, λ_{HP} as m_S, m_{H_0}, v_D, v_H, and α. The reparametrizations for μ_D^2, μ_H^2 and λ_{HP} are given above, while the reparametrization for λ_D and λ_H are

$$\lambda_H = \frac{1}{4v_H^2}\left(m_{H_0}^2 + m_S^2 + (m_{H_0}^2 - m_S^2)\cos 2\alpha\right) \ , \tag{21}$$

$$\lambda_D = \frac{1}{4v_D^2}\left(m_{H_0}^2 + m_S^2 - (m_{H_0}^2 - m_S^2)\cos 2\alpha\right) \ . \tag{22}$$

We also calculate the scalar interactions in the mass eigenstate basis H_0 and S. The cubic scalar interactions are

$$\begin{aligned} \mathcal{L} \supset & - S^3 m_S^2 \frac{v_H \cos^3\alpha + v_D \sin^3\alpha}{2 v_D v_H} - H_0^3 m_{H_0}^2 \frac{v_D \cos^3\alpha - v_H \sin^3\alpha}{2 v_D v_H} \\ & + H_0 S^2 \frac{m_{H_0}^2 + 2m_S^2}{4 v_D v_H}(v_H \cos\alpha - v_D \sin\alpha)\sin 2\alpha \\ & - H_0^2 S \frac{2m_{H_0}^2 + m_S^2}{4 v_D v_H}(v_D \cos\alpha + v_H \sin\alpha)\sin 2\alpha \ . \end{aligned} \tag{23}$$

We have, of course, $m_{H_0} = 125$ GeV and $v_H = 246$ GeV, but the other observables are free parameters. We will restrict $\lambda_{HP} > 0$ in our analysis, recognizing that $\lambda_{HP} < 0$ and $|\lambda_{HP}| > \sqrt{\lambda_H \lambda_D}$ can cause tree-level destabilization of the electroweak vacuum.

Lastly, the scalar-vector-vector interactions of $\tilde{K}$, $\tilde{Z}$, S and H_0 in the mass basis to $\mathcal{O}(\epsilon^2)$ are

$$\begin{aligned}
\mathcal{L} \supset\ & m_{Z,\mathrm{SM}}^2 \left(\frac{\cos\alpha}{v_H} - \epsilon^2 t_W^2 \frac{m_K^2 m_{Z,\mathrm{SM}}^2}{(m_K^2 - m_{Z,\mathrm{SM}}^2)^2} \frac{\sin\alpha}{v_D} \right) \tilde{Z}_\mu \tilde{Z}^\mu H_0 \\
& + 2\epsilon t_W \frac{m_K^2 m_{Z,\ \mathrm{SM}}^2}{(m_{Z,\ \mathrm{SM}}^2 - m_K^2)} \left(\frac{\cos\alpha}{v_H} + \frac{\sin\alpha}{v_D} \right) \tilde{Z}_\mu \tilde{K}_3^\mu H_0 \\
& + m_K^2 \left(-\frac{\sin\alpha}{v_D} + \epsilon^2 t_W^2 \frac{m_K^2 m_{Z,\ \mathrm{SM}}^2}{(m_K^2 - m_{Z,\ \mathrm{SM}}^2)^2} \frac{\cos\alpha}{v_H} \right) \tilde{K}_\mu \tilde{K}^\mu H_0 \\
& + m_{Z,\mathrm{SM}}^2 \left(\frac{\sin\alpha}{v_H} + \epsilon^2 t_W^2 \frac{m_K^2 m_{Z,\ \mathrm{SM}}^2}{(m_K^2 - m_{Z,\ \mathrm{SM}}^2)^2} \frac{\cos\alpha}{v_D} \right) \tilde{Z}_\mu \tilde{Z}^\mu S \\
& + 2\epsilon t_W \frac{m_K^2 m_{Z,\ \mathrm{SM}}^2}{(m_{Z,\ \mathrm{SM}}^2 - m_K^2)} \left(-\frac{\cos\alpha}{v_D} + \frac{\sin\alpha}{v_H} \right) \tilde{Z}_\mu \tilde{K}^\mu S \\
& + m_K^2 \left(\frac{\cos\alpha}{v_D} + \epsilon^2 t_W^2 \frac{m_K^2 m_{Z,\ \mathrm{SM}}^2}{(m_K^2 - m_{Z,\ \mathrm{SM}}^2)^2} \frac{\sin\alpha}{v_H} \right) \tilde{K}_\mu \tilde{K}^\mu S \ . \qquad (24)
\end{aligned}$$

We reiterate that both α and ϵ are theoretical parameters that must be constrained by data, and hence a particular hierarchy between α and ϵ would reflect model-dependent assumptions. As a result, Eq. (24) forms a consistent basis for determining the sensitivity to α and ϵ simultaneously.

We can characterize the changes in the phenomenology of the Higgs-like H_0 state as a combination of modified SM-like production and decay modes and the opening of new exotic production and decay channels. One main effect of α is to suppress all of the SM fermion couplings of the H_0 state by $\cos\alpha$, while the S state acquires Higgs-like couplings to SM fermions proportional to $\sin\alpha$. This feature also applies to the loop-induced couplings to gluons and photons for H_0 and S. On the other hand, the coupling between H_0 to $\tilde{Z}$ bosons is changed not only by $\cos\alpha$ but also by $\epsilon^2 \sin\alpha$, while the S state acquires a $\tilde{Z}$ coupling proportional to $\sin\alpha$ and also $\epsilon^2 \cos\alpha$.

In addition, if kinematically open, the H_0 state can decay to pairs of S or pairs of $\tilde{K}$, with $S \to \tilde{K}\tilde{K} \to 4\chi$ and $\tilde{K} \to \bar{\chi}\chi$ as possible subsequent decays. These Higgs invisible decays are also mimicked by the exotic $H_0 \to \tilde{Z}\tilde{K}$ decay, when $\tilde{Z} \to \bar{\nu}\nu$. As a result, the total invisible width of H_0 is sensitive to a combination of different couplings and masses in Eq. (23) and Eq. (24), further demonstrating the viability of the Double Dark Portal model as a self-consistent theoretical framework for constraining Higgs observables. We remark that we have not added a direct Yukawa coupling between Φ and χ, *e.g.* if Φ has charge +2 under $U(1)_D$, we would introduce a direct decay from S to dark matter and also split the Dirac dark matter into Majorana fermions [46].

C. Dark matter interactions

Finally, we will consider the DM interactions with the mass eigenstates of the gauge bosons and scalars. The main observations can be obtained by recognizing that DM inherits its couplings to SM particles via the J_D current shown in Eq. (15). Explicitly, the dark matter particle Lagrangian reads

$$\mathcal{L} \supset i\bar{\chi}\partial\!\!\!/_\mu \chi + g_D \bar{\chi}\left(\tilde{K}_\mu + \frac{t_W m^2_{Z,\,\mathrm{SM}}}{m^2_K - m^2_{Z,\,\mathrm{SM}}}\epsilon \tilde{Z}_\mu\right)\gamma^\mu \chi - m_\chi \bar{\chi}\chi \ . \tag{25}$$

III. DIRECT DETECTION AND INDIRECT DETECTION PHENOMENOLOGY AND CONSTRAINTS

The Double Dark Portal model presented in Eq. (1) offers many phenomenological opportunities, including dark matter signals at direct detection, indirect detection, and collider experiments and modifications of electroweak precision and Higgs physics at colliders. We remark that aside from the vacuum stability requirement on λ_{HP} and upper bound on $|\epsilon|$, the theory parameter space of the Double Dark Portal model is wide open and subject only to experimental constraints. This vast parameter space has been extremely useful in motivating searches for light, hidden mediators at high intensity, beam-dump experiments, as reviewed in Refs. [25, 42].

Our focus, however, is the $\mathcal{O}(10-100\,\mathrm{GeV})$ scale for the $\tilde{K}$ vector mediator and its accompanying Higgs partner S, which will both dominantly decay to the dark matter particle χ. This is readily motivated by considering $m_\chi < m_{\tilde{K}}/2$ and $g_D \gg \epsilon$, so that $\tilde{K}$ has an on-shell two-body decay to $\bar{\chi}\chi$ and an ϵ^2/g_D^2 suppressed branching ratio to SM charged particles. Moreover, for $m_{\tilde{K}} < m_S/2$ and $\sin\alpha \ll g_D$, the SM gauge singlet scalar S dominantly decays to pairs of $\tilde{K}$ and only have $\sin^2\alpha/g_D^2$ suppressed rates to SM pairs. All of these choices, however, can be reversed to give markedly different phenomenology. If $m_\chi > m_{\tilde{K}}/2$, for example, then the total width of $m_{\tilde{K}}$ scales as ϵ^2 [9] and $\tilde{K}$ decays to pairs of SM charged fermions, as long as it is heavier than $2m_e$. For very small ϵ, however, the $\tilde{K}$ lifetime can be long, leading to either displaced vertex signatures or missing energy signatures. The lifetime and decay length of $\tilde{K}$ can be estimated to be

$$\tau = \frac{1}{\Gamma} = 0.9\times 10^{-2}\ \mathrm{ps}\left(\frac{1\ \mathrm{GeV}}{m_{\tilde{K}}}\right)\left(\frac{10^{-4}}{\epsilon}\right)^2 \frac{1}{\tilde{N}_F}\ , \tag{26}$$

$$L = \gamma c\tau \approx 150\times 10^{-6}\mathrm{m}\left(\frac{1\ \mathrm{GeV}}{m_{\tilde{K}}}\right)\left(\frac{10^{-4}}{\epsilon}\right)^2 \frac{1}{\tilde{N}_F}\ , \tag{27}$$

for $\gamma = 60$ (as from a Higgs two-body decay) and $\tilde{N}_F$ is the effective factor for kinematically open charge-weighted two-body SM final states. If $m_S,\ m_{\tilde{K}} > m_{H_0}/2$, then any possible exotic decay

of the SM-like Higgs will be strongly suppressed by multi-body phase space and a combination of g_D, $\sin\alpha$, or λ_{HP}. We remark that choosing $m_S < m_{H_0}/2$ already gives an exotic Higgs decay, $H_0 \to SS$, which is sensitive directly to λ_{HP}.

Given our mass hierarchy, the dominant collider signature from production of either $\tilde{K}$ or S is missing energy from escaping χ particles, while the relic density of χ in our local dark matter halo can be probed via nuclear recoils in terrestrial direct detection experiments or through their annihilation products in satellite indirect detection experiments. We will discuss the direct and indirect constraints from dark matter searches in the remainder of this section and focus on the collider signatures for vector and scalar mediator production in Sec. IV and Sec. V.

A. Direct detection and relic abundance

Dark matter direct detection experiments search for anomalous nuclear recoil events consistent with the scattering of the dark matter halo surrounding Earth. Direct detection scattering occurs via t-channel exchange of $\tilde{Z}$ and $\tilde{K}$, as evident from the J_D^μ and $J_{\rm em}^\mu$ interactions shown in Eq. (15). Because of the relative sign between the $\tilde{K}$ and $\tilde{Z}$ terms, dark matter scattering proportional to $g^2 g_D^2 \epsilon^2$ is naturally suppressed by extra ϵ^2 or Q^2/m_K^2 factors, where Q is the momentum transfer scale, and the leading contribution is hence proportional to $e^2 g_D^2 \epsilon^2$. This cancellation between $\tilde{K}$ and $\tilde{Z}$ mediators is generic, and we outline the details in Appendix B. As a result, the dominant DM-nucleon interaction for direct detection is mainly from DM-proton scattering. With the SM and DM currents from Eq. (15), the DM-proton scattering cross-section is

$$\sigma_p \simeq \frac{\epsilon^2 g_D^2 e^2}{\pi} \frac{\mu_{\chi p}^2}{m_{\tilde{K}}^4} \approx 10^{-44}\ \text{cm}^2 \left(\frac{g_D}{e}\right)^2 \left(\frac{\epsilon}{10^{-5}}\right)^2 \left(\frac{10\ \text{GeV}}{m_{\tilde{K}}}\right)^2 , \tag{28}$$

where $\mu_{\chi p}$ is the reduced mass of the dark matter χ and the proton and $e = \sqrt{4\pi/137}$. The cross-section σ_p is calculated at leading order in ϵ and $v_{\rm in}$, the incoming DM velocity, and agrees with previous results when DM only interacts via t-channel $\tilde{K}$ exchange with strength proportional to the SM electromagnetic current [37].

Given that the momentum transfer in the propagator is smaller than gauge boson masses $m_{\tilde{K}}$ and $m_{\tilde{Z}}$, then the scattering amplitude is $\mathcal{O}(Q^2/m_V^2)$ suppressed after summing all the vector boson contributions, where m_V is the smaller of either gauge boson mass. For DM direct detection, the momentum transfer is about $Q^2 \sim (m_\chi v_{\rm in})^2 \ll m_{\tilde{K},\tilde{Z}}^2$, hence the contribution induced by the J_Z current cancels and we arrive at the same result in Ref. [37].

We can also motivate particular contours in the ϵ vs. $m_{\tilde{K}}$ plane by considering first the require-

ment that the DM obtains the correct relic density and second the constraints on the possible rates for DM annihilation to SM particles coming from indirect detection experiments. We first calculate the annihilation cross sections for $\chi\bar{\chi} \to f\bar{f}$, W^+W^-, where f denotes a SM fermion. We focus on the region $m_\chi < m_{\tilde{K}}$, since the annihilation channel $\chi\bar{\chi} \to \tilde{K}\tilde{K}$ opens up otherwise and the dominant self-annihilation cross section is insensitive to ϵ.

In this setup, the annihilation cross section will be proportional to $g_D^2\epsilon^2$. We calculate the annihilation in center of mass frame, and give the annihilation cross sections before thermal averaging in Appendix C. We perform the thermal averaging of the annihilation cross section numerically according to Ref. [47]. The annihilation cross section generally has three physical resonances, $m_{\tilde{K}} = 2m_\chi$, $m_{\tilde{Z}} = 2m_\chi$ and $m_{\tilde{K}} = m_{\tilde{Z}}$. The first two resonances are from the s-channel resonant exchange of $\tilde{K}$ and $\tilde{Z}$, while the last one is due to maximal mixing between $\tilde{K}$ and $\tilde{Z}$ when m_K is close to $m_{\mathrm{Z,\,SM}}$, as discussed in Appendix A.

In Fig. 1, we show the direct detection constraints in the ϵ vs. m_K plane from experiments LUX [29] with data from 2013 to 2016, PANDAX-II [28], and CRESST-II [27] as well as CDMS-lite [26] for low mass DM. Each panel shows choices of $g_D = e$, 0.1, and 0.01, and the dark matter mass fixed to $0.2m_K$, $0.495m_K$, 0.6 GeV, or 30 GeV.

The thermal relic abundance limit on ϵ is given in Fig. 1 using the $\Omega h^2 = 0.12$ requirement from the Planck collaboration [30]. The dip around $m_K \sim m_{\mathrm{Z,\,SM}}$ reflects increasing mixing between $\tilde{K}$ and $\tilde{Z}$. While for $m_K \sim 2m_\chi$, the annihilation cross section is enhanced by the s-channel $\tilde{K}$ resonance, thus the required ϵ is very small. When $2m_\chi - m_{\tilde{K}} < T_f$, where $T_f \approx m_\chi/25$ is the DM freeze-out temperature, the annihilation cross section is enhanced by $(m_{\tilde{K}}/T_f)^2$ due to thermal averaging. When $2m_\chi - m_{\tilde{K}} > 0$, the thermal average will not benefit the resonance effect anymore.

In recasting the direct detection limits, we recognize that the experiments assume that the local DM density is fixed to 0.3 GeV/cm^3. Hence, the respective constraints are identically meaningful only when the DDP model parameters give this assumed local relic density. For other parameter space points, in particular for fixed m_K and varying $\epsilon \neq \epsilon_{\mathrm{relic}}$, with $\epsilon_{\mathrm{relic}}$ corresponding to $\langle\sigma v\rangle =$ 0.3 GeV/cm^3, the predicted rate of direct detection scattering events will be independent of ϵ. This is because the predicted local DM relic density will scale with $(\epsilon/\epsilon_{\mathrm{relic}})^2$ while the scattering cross section will scale with $(\epsilon_{\mathrm{relic}}/\epsilon)^2$, leaving the product, and thus the predicted direct detection rate, insensitive to ϵ.

In our recasting, however, we keep the local DM relic density fixed to 0.3 GeV/cm^3 regardless of ϵ, in order to determine the sensitivity to the direct detection cross section. For large ϵ, when the

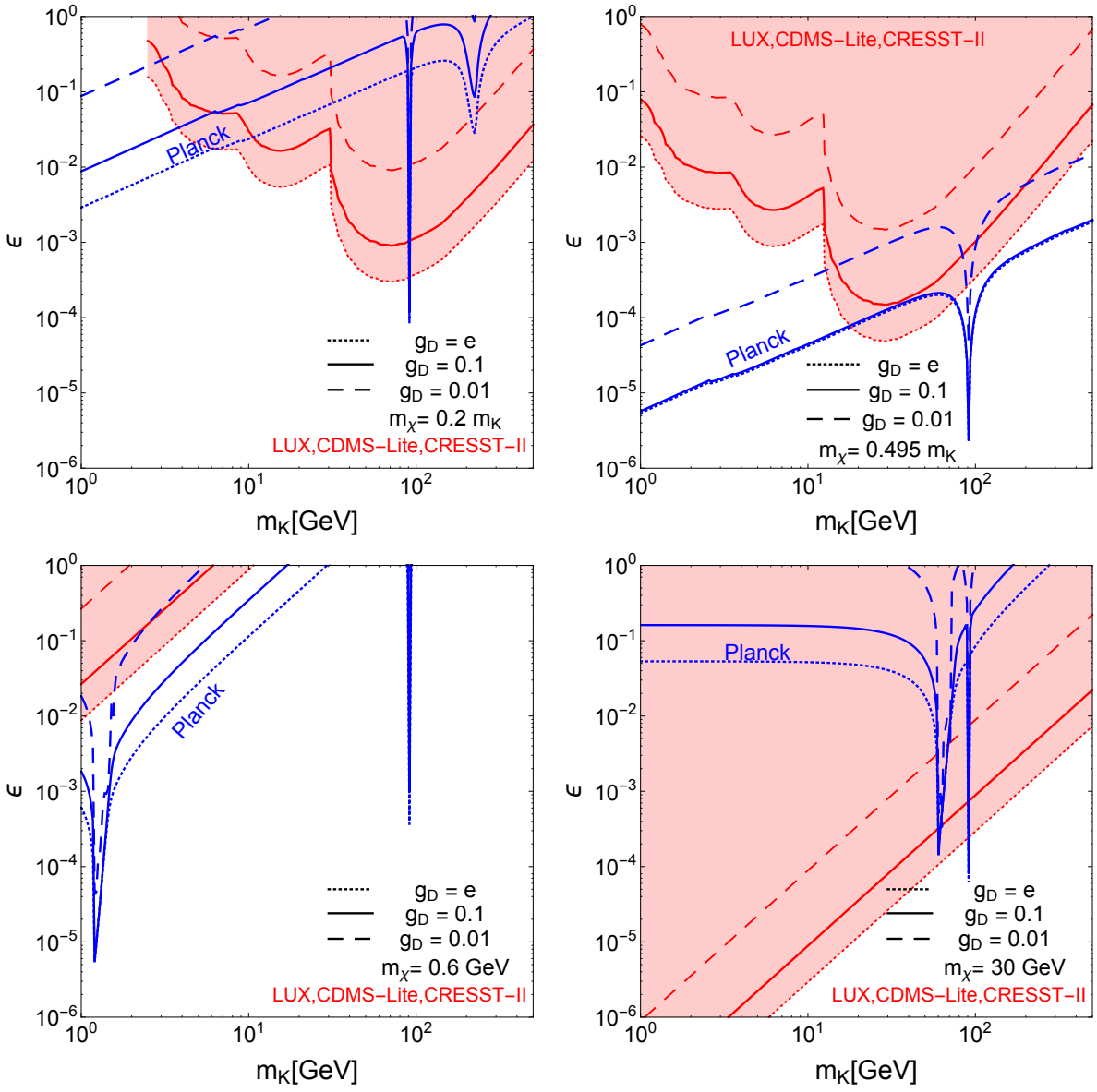

FIG. 1. The leading direct detection constraints from LUX [29], PANDAX-II [28], and CRESST-II [27], as well as CDMSlite [26], shown in the ϵ vs. m_K plane for various choices of g_D and m_χ. We fix $m_\chi = 0.2 m_K$ (top left), $m_\chi = 0.495 m_K$ (top right), $m_\chi = 0.6$ GeV (bottom left), and $m_\chi = 30$ GeV (bottom right), to demonstrate the dependence on the dark matter mass. In each panel, the shaded regions show the exclusions from direct detection experiments for $g_D = e$ (dotted), $g_D = 0.1$ (solid), and $g_D = 0.01$ (dashed), and we overlay blue contours to mark the relic density requirement from the Planck collaboration [30]. Note that m_K is approximately the $m_{\tilde{K}}$ mass eigenvalue according to Eq. (11).

local DM relic density predicted in the DDP model is generally underabundant, extra dark matter particles beyond the DDP model are needed, while for small ϵ, the DM relic density is generally overabundant and extra annihilation channels are typically needed.

Hence, the direct detection exclusion contours in each panel simply illustrate the fractional χ relic density, relative to $\Omega h^2 = 0.12$, that is excluded by the direct detection constraint. When the DD contours are weaker than the relic density contours, the model only minimally requires extra inert dark matter to make up the absent relic abundance. When the DD contours are stronger than the relic density contours, an extra contribution to the thermal relic annihilation cross section for χ is required to satisfy the 0.3 GeV/cm^3 assumption, and ϵ is excluded by DD experiments as shown in the red shaded region. In particular, for fixed m_K, the strengthening to the annihilation cross section can be parametrized by the squared ratio of ϵ from the blue contour to ϵ at the red contour.

We see that light DM masses are much less constrained, because of the $\mu_{\chi p}^2/m_{\tilde{K}}^2$ suppression in Eq. (28). For $m_\chi \propto m_{\tilde{K}}$, the sensitivity on ϵ generally follows the experimental constraint on σ_p. We see that for heavy $\tilde{K}$ and light χ, the direct detection sensitivity can be weak, leaving significant parameter space to be probed by colliders. Interesting parameter space also exists for $m_\chi \lesssim m_{\tilde{K}}/2$, which will be discussed further in the next section.

B. Indirect constraints from CMB, Gamma-ray and $e^\pm$ measurements

After the relic abundance constraint, we next consider the constraints from cosmic microwave background (CMB) observations. Measurements of the CMB generally give constraints on DM annihilation or decay processes, which inject extra energy into the CMB and thus delay recombination [48–53]. The constraint is calculated using the energy deposition yield, $f_{\rm eff}^i$, where i denotes a particular annihilation or decay channel and $f_{\rm eff}$ describes the efficiency of energy absorption by the CMB from the energy released by DM in particular channel. The constraint is expressed as

$$p_{\rm ann} = \frac{1}{m_\chi} \sum_i f_{\rm eff}^i \langle \sigma v \rangle_i \ , \tag{29}$$

where the Planck experiment has constrained $p_{\rm ann} < 4.1 \times 10^{-28}$ cm^3 s^{-1} GeV^{-1} [30], and we sum all the SM fermion pair $\bar{f}f$ and W^+W^- channels in annihilation. The excluded parameters are plotted in Fig. 2 as shaded green regions.

The next constraints we consider are the gamma ray observations from Fermi-LAT and MAGIC in dwarf galaxies [31, 32]. In Ref. [31], Fermi-LAT gives constraints on e^+e^-, $\mu^+\mu^-$, $\tau^+\tau^-$, $\bar{u}u$, $\bar{b}b$ and W^+W^- final states, while in Ref. [32], MAGIC has made a combined analysis with Fermi-LAT and presented constraints on $\mu^+\mu^-$, $\tau^+\tau^-$, $\bar{b}b$ and W^+W^-. The computation of constraints on our model is straightforward, since we can calculate each individual limit on ϵ for each channel

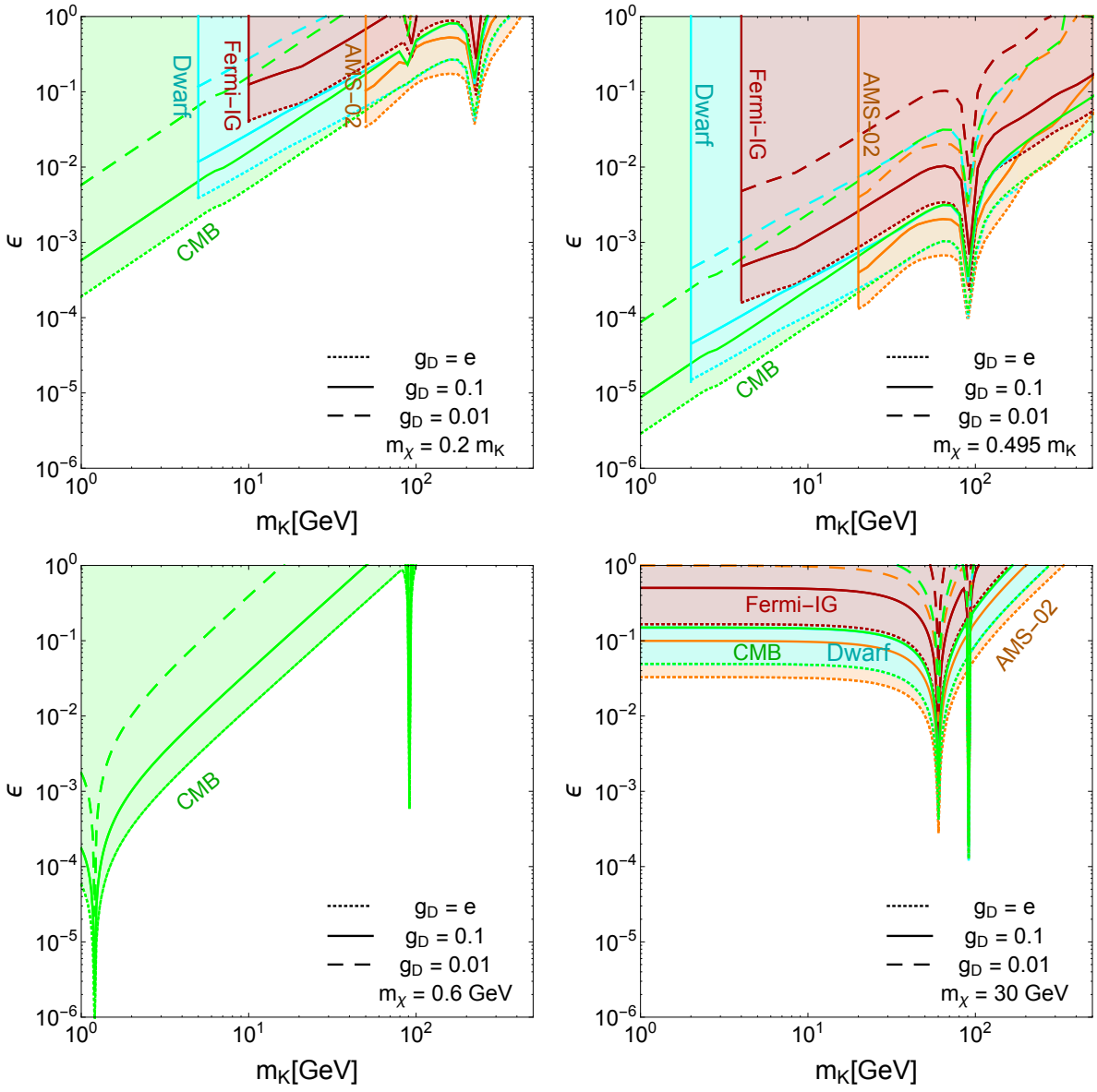

FIG. 2. The indirect detection constraints from CMB measurements [30], gamma-ray measurements from dwarf galaxies [31, 32] and the inner galactic region [33] and e^+ flux measurement from AMS-02 [34]. The constraints are shown in the ϵ vs. m_K plane for $m_\chi = 0.2\ m_K$ (top left), $0.495\ m_K$ (top right), 0.6 GeV (bottom left), and 30 GeV (bottom right), with $g_D = e$ (dotted), 0.1 (solid), and 0.01 (dashed). Note that m_K is approximately the $m_{\tilde{K}}$ mass eigenvalue according to Eq. (11).

and take the most stringent constraint for each m_χ mass. The excluded parameter region is shaded by cyan in Fig. 2. Similarly, we consider the gamma ray constraints from the inner Milky way [33]. This analysis sets conservative constraints on various SM final states by using the inclusive photon spectrum observed by the Fermi-LAT satellite. We apply their results by calculating the most stringent annihilation profile, assuming the Navarro-Frenk-White profile for the DM density

distribution in the galactic center [54]. We can see in Fig. 2 that the constraint from galactic center region, shaded in dark red, is much weaker than that from dwarf galaxies.

The last indirect detection constraint is based on e^+ and e^- data from the AMS-02 satellite [34]. We use the constraints from Ref. [55] to set bounds on various SM final states, which mainly derive from the observed positron flux. We again adopt the limits from the strongest channel to constrain ϵ for each mass parameter choice. We can see the constraint from AMS-02 is the strongest at the largest m_χ masses in Fig. 2.

To summarize, in Fig. 2, we see that the CMB constraint is strongest at small m_χ, while AMS-02 is strongest at higher m_χ. The constraint from gamma ray observations in dwarf galaxies is very close to the CMB constraint. Meanwhile, the dips in Fig. 2 nicely show the two s-channel resonances of $\tilde{K}$ and $\tilde{Z}$ as well as the maximal mixing peak between $\tilde{K}$ and $\tilde{Z}$.

IV. COLLIDER PHENOMENOLOGY OF THE DOUBLE DARK PORTAL MODEL AND CURRENT CONSTRAINTS FROM LEP AND LHC

In this section, we give an overview of the possible probes of the Double Dark Portal Model at both lepton and hadron colliders. While many separate searches have been performed at LEP and LHC experiments in the context of either kinetic mixing or Higgs mixing scenarios, we highlight the fact that a future e^+e^- machine must synthesize both effects in any given search. Hence, the Double Dark Portal model is a natural framework to study light, hidden physics at a future e^+e^- machine.

The Double Dark Portal model motivates observable deviations in measurements of both the SM-like H_0 and the $\tilde{Z}$ bosons, which test the scalar mixing angle α as well as the kinetic mixing parameter ϵ. Notably, the primary SM Higgsstrahlung workhorse process at an e^+e^- Higgs factory, $e^+e^- \to Zh$, can deviate significantly from the SM expectation for nonzero ϵ or α. For instance, nonzero α causes a well-known $\cos\alpha$ suppression of the $H_0\tilde{Z}_\mu\tilde{Z}^\mu$ vertex, but nonzero ϵ gives an additional diagram with intermediate $\tilde{K}$, which becomes on-shell when $m_{\tilde{K}} > m_{\tilde{Z}} + m_{H_0}$. We remark that these effects are not generically captured by a simple $\cos\alpha$ rescaling of the $H_0\tilde{Z}_\mu\tilde{Z}^\mu$ vertex.

In Fig. 3, we show the new possibilities for SM-like and dark scalar Higgsstrahlung from the intermediate massive vector bosons $\tilde{K}$ and $\tilde{Z}$. We also show the radiative return process for $e^+e^- \to \tilde{A}\tilde{K}$ or $\tilde{A}\tilde{Z}$, and the diboson process $e^+e^- \to \tilde{K}\tilde{Z}$. All of these processes give different signals at a future e^+e^- machine. If we also consider the possibility of Z-pole measurements and

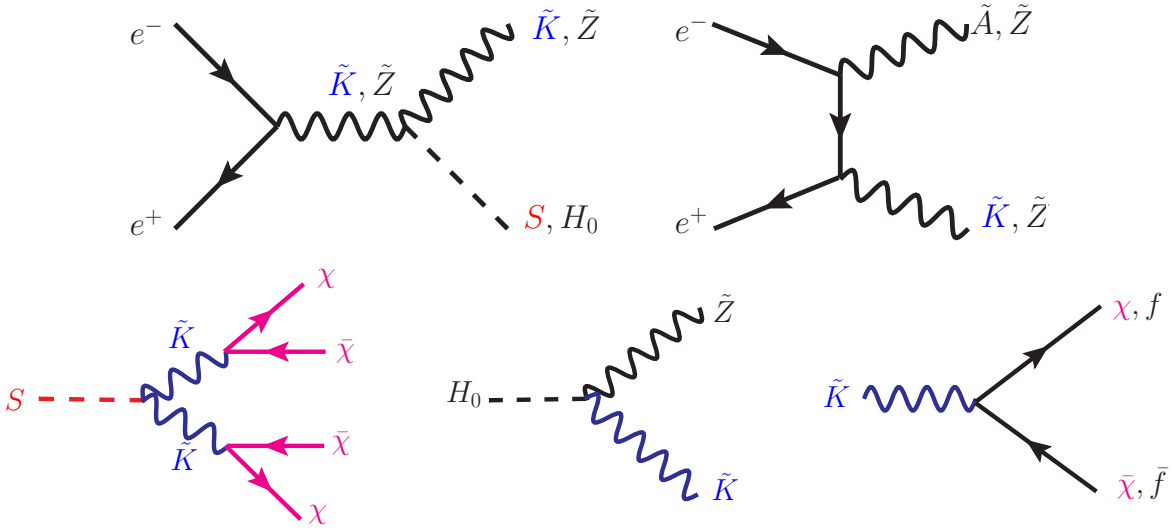

FIG. 3. Feynman diagrams for (top left) vector + scalar production, (top right) vector + vector production and (bottom row) example new decay processes in the Double Dark Portal model sensitive to the kinetic mixing ϵ and scalar Higgs λ_{HP} portal couplings. Note $\tilde{Z}$, $\tilde{A}$, and H_0 are the mass eigenstates corresponding to the SM-like Z, photon, and Higgs bosons, respectively.

Drell-Yan processes probing Eq. (15), then we can categorize the collider phenomenology of the Double Dark Portal model into four groups: electroweak precision and Z-pole observables, Higgs measurements, Drell-Yan measurements, and radiative return processes. We point out, however, that e^+e^- machines offer unique opportunities for probing new, light, hidden particles by virtue of the recoil mass method, which we discuss first.

A. Recoil mass method for probing new, light, hidden states

As long as they are kinematically accessible, both S and $\tilde{K}$ can be produced in e^+e^- collisions in association with SM particles. Hence, even if they decay invisibly, the recoil mass method can be used to probe the couplings $\sin\alpha$ and ϵ, according to the interactions from Eq. (15) and Eq. (24). This is familiar from the leading $e^+e^- \to \tilde{Z}H_0$ Higgsstrahlung production process, where the reconstruction of the $\tilde{Z} \to \ell^+\ell^-$ decay consistent with a 125 GeV recoil mass gives a rate dependent only on the $H_0\tilde{Z}_\mu\tilde{Z}^\mu$ coupling. We emphasize (see also Ref. [56]) that this generalizes to any scattering process at an e^+e^- machine if visible SM states are produced in association with a new, light, hidden particle. Moreover, sensitivity to the hidden states S and $\tilde{K}$ can be improved by scanning over $\sqrt{s}$, where the various production modes of $\tilde{Z}S$, $\gamma\tilde{K}$, and $\tilde{Z}\tilde{K}$ can be optimized for the different S and $\tilde{K}$ masses. This $\sqrt{s}$ adjustment would be immediately motivated, for example,

by a new physics signal in the recoil mass distribution.

The recoil mass method uses the knowledge that the center-of-mass frame for the e^+e^- collision is fixed to be $(\sqrt{s}, 0, 0, 0)$ in the lab frame, where $\sqrt{s}$ is the energy of the collider. Hence, for an invisibly decaying final state particle X produced in association with a SM state Y, four-momentum conservation requires

$$E_Y = \frac{\sqrt{s}}{2} + \frac{m_Y^2 - m_X^2}{2\sqrt{s}} \ , \tag{30}$$

or equivalently,

$$m_X = \sqrt{s + m_Y^2 - 2E_Y\sqrt{s}} \ . \tag{31}$$

If there are multiple visible states Y_i, this generalizes to

$$\sum E_{Y_i} = \frac{\sqrt{s}}{2} + \frac{(\sum p_i)^2 - m_X^2}{2\sqrt{s}} \ , \quad m_X = \sqrt{s + (\sum p_i)^2 - 2(\sum E_{Y_i})\sqrt{s}} \ , \tag{32}$$

where $(\sum p_i)^2$ is the total invariant mass of the Y_i system. We see that studying the differential distribution of E_Y will show a characteristic excess at a given E_Y when X is produced. Identifying this monochromatic peak is formally equivalent to finding a peak in the recoil mass distribution, but we emphasize that these two distributions reconstructed differently at e^+e^- colliders. Specifically, the recoil mass distribution uses both the energy and total four-momentum of each detected SM particle, which the differential energy distribution only requires calorimeter information.

In particular, for the $\tilde{Z}H_0$, $\tilde{Z} \to \ell^+\ell^-$ Higgsstrahlung process, the recoil mass method requires measurements of each individual lepton four-momentum and the event-by-event invariant mass $m_{\ell\ell}$. The resulting differential distribution also includes off-shell contributions and interference, giving a smeared peak in the recoil mass distribution whose width is dominated by experimental resolution and not the intrinsic Higgs width. On the other hand, in radiative return processes, both the recoil mass distribution and the photon energy spectrum are only limited by the possible width of the recoiling new physics particle and the photon energy resolution.

For our studies, we assume both S and $\tilde{K}$ have dominant decay widths to the dark matter χ, which does not leave tracks or calorimeter energy deposits as it escapes. The recoil mass technique, however, also readily probes both the $\tilde{K}$ and S masses in numerous production modes, when we produce $\tilde{K}$ or S in association with a visible SM final state. For example, while the SM-like $\tilde{Z}$ boson is a canonical choice to study $\tilde{Z}H_0$ events, we can use the recoil mass technique in the radiative return process for $\tilde{A}\tilde{K}$ production to identify the invisible decay of $\tilde{K}$. An even more striking possibility is to use the SM-like Higgs boson, H_0, as the recoil mass particle to probe $\tilde{K}H_0$ production.

B. Modifications to electroweak precision

We now consider the four categories of collider processes in turn. The first set of observables we consider are those from electroweak precision tests. In the Double Dark Portal model, Z-pole observables will show deviations according to the new decay channel $\tilde{Z} \to \bar{\chi}\chi$ or $\tilde{Z} \to S\tilde{K}$, sensitive to ϵ, shifts in the $\tilde{Z}$ mass from the mixing with $\tilde{K}$, and deviations in the weak mixing angle from the mixing between $\tilde{K}$, $\tilde{A}$, and $\tilde{Z}$. In particular, identifying the $\tilde{Z}$ mass eigenstate of the DDP as the 91.2 GeV Z boson studied by LEP, measurements of the Z mass, total width, and the invisible decay to SM neutrinos give strong constraints on ϵ and the possibility of exotic decays. For $m_{\tilde{K}} < 10$ GeV, both the visible and invisible channels can be constrained by various experiments, as reviewed in Ref. [25]. We thus focus on the status and prospects for $m_{\tilde{K}} > 10$ GeV.

1. LEP-I and LEP-II constraints

At LEP-II, contact operators $(4\pi/\Lambda^2)\bar{e}\gamma^\mu e\bar{f}\gamma_\mu f$ were used to test for new physics, analogous to angular distributions in dijet studies at the LHC. In the $e^+e^- \to \ell^+\ell^-$ channel, the constraint on Λ is $\gtrsim 20$ TeV [57]. The non-observation of direct s-channel exchange of $\tilde{K}$ then requires $\epsilon/m_{\tilde{K}} \lesssim 4 \times 10^{-3}$ GeV^{-1}, if the invisible decay of $\tilde{K}$ is neglected.

As mentioned above, the mixing between $Z_{\rm SM}$ and K leads to shifts in the $\tilde{Z}$ mass and couplings to SM fermions, leading to a constraint of $\epsilon < 0.03$ for $m_{\tilde{K}} < m_Z$ using a combination of electroweak precision observables [8]. The constraint is weakened for $m_{\tilde{K}} > m_Z$ where the limit on ϵ is about 0.1 at $m_{\tilde{K}} = 200$ GeV [8].

Although the canonical SM Higgs production channel $e^+e^- \to Zh$ was ineffectual at LEP-II, the scalar mixing angle $\sin\alpha$ can still be probed by the $e^+e^- \to \tilde{Z}S$ production mode when S is kinematically accessible by LEP-II. For $m_S < 114$ GeV, the non-observation of Higgs-like scalar decays constrains $\sin^2\alpha < \mathcal{O}(0.01 - 0.1)$ [20], as long as the $S \to \tilde{K}\tilde{K}$ decay is turned off.

The LEP experiments have also searched for a low mass Higgs in the exotic $Z \to HZ^\star$ decay, with $Z^\star \to \ell^+\ell^-$ and H decaying invisibly, which excludes $m_H < 66.7$ GeV if the invisible branching fraction is 100% [16]. The ZH Higgsstrahlung process is also used to push the mass exclusion to 114.4 GeV [17–19], although the intermediate mass range between these two limits are not comprehensively covered. In our model, $S \to \tilde{K}\tilde{K}$ is the dominant decay when $g_D \gg \sin\alpha$, and the decay branching fraction $\tilde{Z} \to S\tilde{Z}^\star$ and the production cross section $\sigma(\tilde{Z}S)$ are hence $\sin^2\alpha$ suppressed compared to the SM rate. Therefore, these limits apply to S as bounds on $\sin\alpha$ and

m_S, which we will show in Fig. 7 in Sec. V. Note the constraint from the exotic $\tilde{Z} \to S\tilde{Z}^\star$ decay is much stronger than $\tilde{Z}H_0$ Higgsstrahlung process in Fig. 7 due to the high statistics of Z decays, and in the calculation we accounted for the subsequent decay branching fractions of $\mathrm{BR}(S \to \tilde{K}\tilde{K})$ and $\mathrm{BR}(\tilde{K} \to \bar{\chi}\chi)$.

C. Modifications to Higgs physics and LHC constraints

With the era of precision Higgs characterization underway after the discovery of a Higgs-like boson [58, 59], the ATLAS and CMS collaborations have provided the strongest constraints on the possible mixing of the SM Higgs boson with a new gauge singlet ϕ. In addition, searches for an invisible decay of the 125 GeV Higgs boson, sensitive to $H_0 \to SS$ or $H_0 \to \tilde{K}\tilde{K}$ decays, have also given constraints on λ_{HP}, $\sin\alpha$, and ϵ. The growing Higgs dataset at the LHC continues to show no significant deviations from the SM expectation, but the current sensitivity of the LHC experiments to our proposed signals is limited.

The most important constraint comes from the search for an invisible decay of the 125 GeV Higgs, where the Run 1 combination of ATLAS and CMS data constrains $\mathrm{BR}(h \to \text{ inv}) \leq 0.23$ [60, 61]. We highlight, however, that this limit requires that the Higgs is produced in the $\tilde{Z}H_0$ and vector boson fusion processes at SM rates, which is violated in the DDP model. Moreover, in the DDP model, there are two possible direct invisible decays, $H_0 \to SS \to 4\tilde{K} \to 8\chi$ and $H_0 \to 2\tilde{K} \to 4\chi$, in addition to the possible exotic decay $H_0 \to \tilde{Z}\tilde{K} \to \bar{\nu}\nu\bar{\chi}\chi$, which is often semi-visible. The $H_0 \to SS$, $H_0 \to \tilde{K}\tilde{K}$ and $H_0 \to \tilde{K}\tilde{Z}$ decay widths at leading order in ϵ and α are

$$\Gamma(H_0 \to SS) = g_D^2 \sin^2\alpha \frac{m_{H_0}}{32\pi}\sqrt{1-\frac{4m_S^2}{m_{H_0}^2}}\frac{(m_{H_0}^2+2m_S^2)^2}{m_{H_0}^2 m_K^2}\ , \tag{33}$$

$$\Gamma(H_0 \to \tilde{K}\tilde{K}) = g_D^2 \sin^2\alpha \frac{m_{H_0}}{32\pi}\sqrt{1-\frac{4m_{\tilde{K}}^2}{m_{H_0}^2}}\frac{m_{H_0}^4-4m_{H_0}^2m_{\tilde{K}}^2+12m_{\tilde{K}}^4}{m_{H_0}^2 m_{\tilde{K}}^2}\frac{m_K^2}{m_{\tilde{K}}^2}\ , \tag{34}$$

$$\begin{aligned}\Gamma(H_0 \to \tilde{K}\tilde{Z}) = {} & \frac{\epsilon^2 t_W^2\left(\frac{\cos\alpha}{v_H}+\frac{\sin\alpha}{v_D}\right)^2}{16\pi m_{H_0}^3\left(m_K^2-m_{Z,\,\mathrm{SM}}^2\right)^2}\frac{m_K^4 m_{Z,\,\mathrm{SM}}^4}{m_{\tilde{K}}^2 m_{\tilde{Z}}^2}\sqrt{m_{H_0}^4+\left(m_{\tilde{K}}^2-m_{\tilde{Z}}^2\right)^2-2m_{H_0}^2\left(m_{\tilde{K}}^2+m_{\tilde{Z}}^2\right)} \\ & \times\left((m_{H_0}^2-m_{\tilde{K}}^2-m_{\tilde{Z}}^2)^2+8m_{\tilde{K}}^2m_{\tilde{Z}}^2\right)\ .\end{aligned} \tag{35}$$

The first two decay widths are proportional to m_K^{-2} while the last one is proportional to m_K^2, therefore the last one is usually much smaller comparing with the first two when m_K is light. In the Higgs invisible studies, the experiments will constrain the rate for Higgs invisible decays in the

DDP model,

$$\mathrm{BR}_{\mathrm{inv}}^{\mathrm{eff}} = \frac{\sigma(\tilde{Z}H_0)}{\sigma_{\mathrm{SM}}(Zh)} \times \mathrm{BR}(H_0 \to \mathrm{inv}) = \cos^2\alpha \frac{1}{\Gamma_{H_0,\,\mathrm{tot}}} \Big(\Gamma(H_0 \to SS)\mathrm{BR}^2(S \to \tilde{K}\tilde{K})\mathrm{BR}^4(\tilde{K} \to \bar{\chi}\chi) + \Gamma(H_0 \to \tilde{K}\tilde{K})\mathrm{BR}^2(\tilde{K} \to \bar{\chi}\chi) + \Gamma(H_0 \to \tilde{K}\tilde{Z})\mathrm{BR}(\tilde{K} \to \bar{\chi}\chi)\mathrm{BR}(\tilde{Z} \to \bar{\nu}\nu) \Big) \ , \tag{36}$$

where $\Gamma_{H_0,\,\mathrm{tot}} = \cos^2\alpha\Gamma_{h,\,\mathrm{SM}} + \Gamma(H_0 \to SS) + \Gamma(H_0 \to \tilde{K}\tilde{K}) + \Gamma(H_0 \to \tilde{K}\tilde{Z})$. The decay widths $\tilde{K} \to \bar{f}f$, W^+W^- can be found in the appendix of Ref. [62], while the decay width $\tilde{K} \to \bar{\chi}\chi$ is

$$\Gamma(\tilde{K} \to \bar{\chi}\chi) = \frac{g_D^2}{12\pi}\sqrt{m_{\tilde{K}}^2 - 4m_\chi^2}\left(1 + \frac{2m_\chi^2}{m_{\tilde{K}}^2}\right) . \tag{37}$$

The prediction for the invisible decay branching fraction of the 125 GeV Higgs is shown in the left and middle panels of Fig. 4 in the $\sin\alpha$ vs. ϵ plane for $m_S = 50$ GeV, $m_K = 20$ GeV, and $g_D = e$, 0.01. The current constraint of $\mathrm{BR}_{\mathrm{inv}} < 0.23$ is adopted from Refs. [60, 61], while the prospective sensitivity of $\mathrm{BR}_{\mathrm{inv}} < 0.005$ is adopted from the estimate using 10 ab^{-1} of $\sqrt{s} = 240$ GeV data using unpolarized beams in Ref. [3]. This prospective limit can be lowered in combined fits, with more luminosity, or with other assumptions about detector performance to the $\mathcal{O}(0.001)$ level [1, 2, 4].

In Fig. 4, we see that when g_D is large, the sensitivity to $\sin\alpha$ is much stronger than ϵ, because the decay widths for $H_0 \to SS$ and $H_0 \to \tilde{K}\tilde{K}$ are much larger than $H_0 \to \tilde{K}\tilde{Z}$ due to light m_K, as discussed previously. More importantly, for large g_D, $\mathrm{BR}(S \to \tilde{K}\tilde{K})$ and $\mathrm{BR}(\tilde{K} \to \bar{\chi}\chi)$ are close to 100%. When $g_D < \sin\alpha$ or $g_D < \epsilon$, $\mathrm{BR}(S \to \tilde{K}\tilde{K})$ and $\mathrm{BR}(\tilde{K} \to \bar{\chi}\chi)$ will both be subdominant and result in the decrease of $\mathrm{BR}_{\mathrm{inv}}^{\mathrm{eff}}$ as in the middle panel of Fig. 4. As shown in the right panel of Fig. 4, the constraint on $\sin\alpha$ from invisible Higgs decays can be relaxed by making g_D smaller.

These exotic decays can also give fully visible and semi-visible signatures [8, 63–66] when the $\tilde{K}$ or S particle decays to SM final states, which provide additional handles for Higgs collider phenomenology. Those references concentrate on the scenario where the decay to SM final states are dominant, *e.g.* $m_{\tilde{K}} < 2m_\chi$. Therefore, such constraints should be modified by the relevant branching ratios in the DDP model because the DDP model includes a DM decay. If visible decays of $\tilde{K}$ dominate, though, the search for $h \to 2a \to 4\mu$ [67] constrains the process $H_0 \to \tilde{K}\tilde{K}$, and bounds $\lambda'_{HP} \lesssim 0.01$ for $m_{\tilde{K}} \lesssim 10$ GeV [8], while the bound strengthens to $\lambda'_{HP} \lesssim 0.001$ [8] for $m_{\tilde{K}} \gtrsim 10$ GeV from recasting the differential distributions in 8 TeV $h \to ZZ^* \to 4\ell$ data [68]. The coupling $\lambda'_{HP} = \lambda_{HP}m_{H_0}^2/|m_{H_0}^2 - m_S^2|$, is roughly the same as λ_{HP} if m_S is not close to or much larger than m_{H_0}. The high luminosity LHC (HL-LHC) with 3 ab^{-1} of 14 TeV luminosity is expected to be sensitive to $\lambda'_{HP} \lesssim (\mathrm{few}) \times 10^{-5}$ in this same channel, depending on the $m_{\tilde{K}}$ mass. The four lepton final state has also been used to constrain the exotic decay $H_0 \to \tilde{Z}\tilde{K}$,

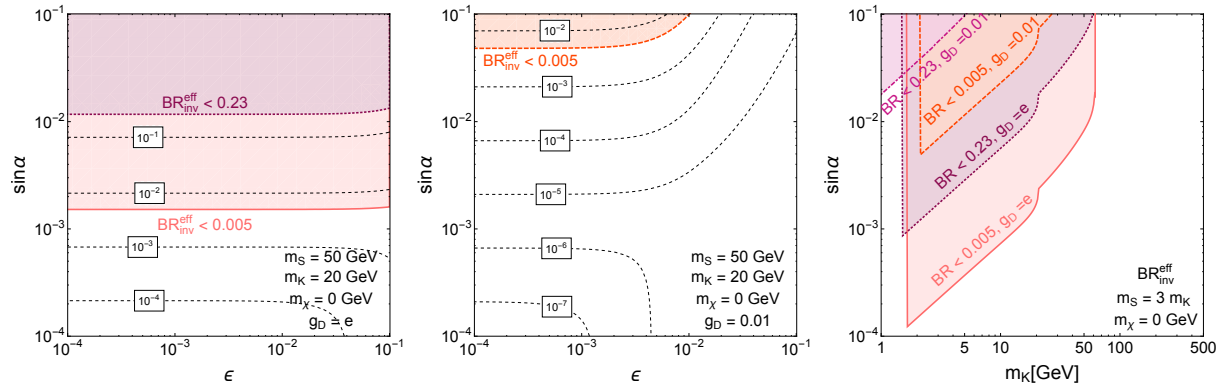

FIG. 4. (Left and middle panel) Rates for the invisible branching fraction of the 125 GeV Higgs in the $\sin\alpha$ vs. ϵ plane, setting $m_S = 50$ GeV, $m_K = 20$ GeV, and $g_D = e$ (left) and 0.01 (middle). (Right panel) Exclusion regions in the $\sin\alpha$ vs. m_K plane from the search for an invisible decay of the 125 GeV Higgs by ATLAS and CMS giving $\mathrm{BR}_{\mathrm{inv}} < 0.23$ [60, 61], and projected reach from a future e^+e^- machine giving $\mathrm{BR}_{\mathrm{inv}} < 0.005$ [1–4].

which gives sensitivity to ϵ from (24). The current bound using 8 TeV data is weak, with the strongest sensitivity for $m_{\tilde{K}} \approx 30$ GeV giving $\epsilon \lesssim 0.05$, while the improvement at the HL-LHC is expected to reach $\epsilon \lesssim 0.01$ [8]. These gains are mainly limited by the statistics afforded by Higgs production rates. We remark that for very small ϵ and $m_\chi > m_{\tilde{K}}/2$, as discussed in Sec. III, the hidden photon will have a displaced decay to SM states, which provides a new set of challenges to trigger and detect at colliders. Current exclusions and future prospects for displaced decays can be found, *e.g.*, in Refs. [8, 25, 42].

1. *Modifications to Drell-Yan processes*

The $\tilde{K}$ decay to SM final states can be dominant, if the decay to DM pairs is kinematically forbidden or $g_D \ll \epsilon$. In this case, at the LHC, the Drell-Yan process $pp \to \tilde{Z}, \tilde{K} \to \ell^+\ell^-$ can be used to constrain the kinetic mixing parameter ϵ, since this process has been studied with exquisite precision by the ATLAS and CMS experiments. Both ATLAS and CMS have searched for dilepton resonances at high mass, $m_{\tilde{K}} \gtrsim 200$ GeV, using 20 fb^{-1} of 8 TeV data [69, 70], which restricts $\epsilon \lesssim 0.01$ at $m_{\tilde{K}} = 200$ GeV and weakens to $\epsilon \lesssim 0.05$ at $m_{\tilde{K}} = 1000$ GeV [71, 72]. For $m_{\tilde{K}}$ between 10 and 80 GeV, the Drell-Yan search using 7 TeV data by CMS [73] and the corresponding sensitivity using 8 TeV data gives $\epsilon \lesssim 0.005$, stronger than the current electroweak precision constraints [72].

The HL-LHC is expected to constrain $\epsilon \lesssim 0.001$ for $m_{\tilde{K}}$ between 10 and 80 GeV using Drell-Yan

data, while high mass $\tilde{K}$ can be probed at the $\epsilon \sim 0.002$ level for $m_{\tilde{K}} = 200$ GeV and the $\epsilon \sim 0.01$ level for $m_{\tilde{K}} = 1000$ GeV. The recent 13 TeV, 3.2 fb^{-1} search for high mass dilepton resonances by ATLAS [74] also constrains the kinetic mixing parameter $\epsilon \lesssim 0.04$ for $m_{\tilde{K}} > 100$ GeV [75], but this result is hampered by the small statistics. We see that as long as $\tilde{K}$ has an appreciable branching fraction to SM final states, in particular leptons, the Drell-Yan process at the LHC and HL-LHC will provide stronger sensitivity to ϵ compared to electroweak precision observables. For $g_D/\epsilon \gg 1$, the decay $\tilde{K} \to \bar{\chi}\chi$ is dominant and the situation reverses, and then Drell-Yan constraints will not compete with the electroweak precision observables.

2. Radiative return processes and dark matter production at the LHC

The radiative return process, $e^+e^- \to \gamma X$, enables on-shell production of new particles at fixed $\sqrt{s}$ colliders by using an extra radiated photon to conserve four-momentum. At hadron colliders, since the colliding objects are composite, dark matter production via radiative return is more commonly known as monojet or monophoton processes, recognizing the fact that the partonic center of mass energy is not constant on an event-by-event basis.

As a result, the visible decays $\tilde{K} \to \ell^+\ell^-$ discussed in the Higgs to four leptons and the Drell-Yan contexts are complemented by the LHC searches for dark matter production in monojet and monophoton processes. We remark that in our DDP model, we will assume that $\tilde{K} \to \bar{\chi}\chi$ is the dominant decay channel, leading to an overall ϵ^2/g_D^2 suppression in the above visible decay rates. Both ATLAS and CMS have searches for dark matter production using 8 TeV data [76, 77], sensitive to mediator masses as low as 10 GeV [76]. The corresponding 13 TeV searches [35, 36] have yet to achieve the same sensivity at low masses. In the DDP model, the $\tilde{K}$ mediator is produced on-shell and decays dominantly to $\bar{\chi}\chi$, and calculating the results for on-shell mediator production at the LHC, we obtain $\epsilon \lesssim 0.07$, similar to previous studies [78–80]. It is also possible to search for the dark bremsstrahlung of $\tilde{K}$ from the DM pair [81, 82], as a probe of ϵ, although these rates are negligible in our model.

V. PROSPECTS FOR FUTURE COLLIDERS

We have established that significant room remains to be explored in both the ϵ and λ_{HP} portal couplings. We will now demonstrate that a future e^+e^- collider, currently envisioned as a Higgs factory, will have leading sensitivity to probing both couplings simultaneously through the production

of new, light, hidden states $\tilde{K}$ and S. The primary motivation for the $\sqrt{s} \sim 240 - 250$ GeV center-of-mass energy of such a collider is to optimize the expected $\sigma(e^+e^- \to Zh)$ SM Higgsstrahlung cross section, taking into account the possible polarization of the incoming electron-positron beams. Such high energies, however, also enable production of the new states $\tilde{K}$ and S from radiative return processes, exotic Higgs decays, and exotic Higgsstrahlung diagrams.

A few different variations exist for next-generation e^+e^- machines, namely the International Linear Collider (ILC) [2], an e^+e^- Future Circular Collider (FCC-ee), which shares strong overlap with TLEP [3], or a Circular Electron-Positron Collider (CEPC) [4]. Since the physics we discuss will only depend very mildly on the particular $\sqrt{s}$ of the future machine and possible polarization of the incoming electron and positron beams, we will adopt a $\sqrt{s} = 250$ GeV machine colliding unpolarized e^+ and e^- beams as our reference machine with a total integrated luminosity of $L = 5$ ab^{-1} in our collider studies. For comparison, we also show future expectations for a possible $\sqrt{s} = 500$ GeV machine with $L = 5$ ab^{-1} total integrated luminosity. Our work will complement and extend previous ϵ and $\sin\alpha$ sensitivity estimates made for various specific collider environments, which we review first.

A. Electroweak precision tests, Higgsstrahlung, and invisible Higgs decays at future e^+e^- colliders

Because the SM Z and the dark vector K mix, the $\tilde{Z}$ mass eigenstate develops a new invisible decay channel, $\tilde{Z} \to \bar{\chi}\chi$, if kinematically allowed. This invisible decay width can be accurately measured at a future e^+e^- machine. At FCC-ee, for example, running on the W^+W^- threshold using the radiative return process $e^+e^- \to Z\gamma$ ($L_{\rm int} = 15.2$ ab^{-1}), complemented by additional runs at $\sqrt{s} = 240$ GeV ($L_{\rm int} = 10.44$ ab^{-1}) and $\sqrt{s} = 350$ GeV ($L_{\rm int} = 0.42$ ab^{-1}), can constrain the number of active neutrino species, assuming statistical uncertainties, down to $\Delta N_\nu \approx 0.001$ [83, 84]. This leads to the possible constraint $\epsilon < 0.01$ for $m_{\tilde{K}} < m_{\tilde{Z}}/2$. Measurements directly on the Z-pole are not expected to compete with this constraint because of theory uncertainties on the small-angle Bhabha-scattering cross section remain too large [83]. This constraint also applies to the $\tilde{Z} \to \tilde{K}S \to 6\chi$ exotic decay, if $m_{\tilde{K}} + m_S < m_{\tilde{Z}}$. For a lepton collider running on the Z-pole, though, other electroweak precision observables will have greatly enhanced precision. The combination of improved electroweak precision observables can constrain $\epsilon \lesssim 0.004$ for $m_{\tilde{K}} < m_{\tilde{Z}}$, although the ϵ constraint is much weaker for $m_{\tilde{K}} > m_{\tilde{Z}}$ [8].

The e^+e^- Higgs factory is expected to have a precision measurement of the Higgsstrahlung

process $e^+e^- \to Zh$, with accuracies ranging from $\mathcal{O}(0.3\% - 0.7\%)$ expected, using $5 - 10$ ab^{-1} of luminosity [3, 4, 85]. These rates imply that the scalar mixing angle is probed to $\sin\alpha \lesssim 0.055 - 0.084$, simply from the observation of the Higgsstrahlung process.

Aside from precision Higgs measurements, a future e^+e^- machine will have leading sensitivity to an invisible decay of the 125 GeV Higgs. As reviewed in Subsec. IV C, the current constraint on the Higgs invisible decay branching ratio is $\text{BR}_{\text{inv}} < 0.23$ [60, 61], while the limit at FCC-ee is expected to be $\text{BR}_{\text{inv}} < 0.005$ [3]. We have discussed the two main invisible decays, $H_0 \to SS \to 8\chi$ and $H_0 \to \tilde{K}\tilde{K} \to 4\chi$, as well as the irreducible signal from $H_0 \to \tilde{Z}\tilde{K} \to \bar{\nu}\nu\bar{\chi}\chi$ in Subsec. IV C. We also show the corresponding sensivity in the $\sin\alpha$ vs. ϵ and $\sin\alpha$ vs. $m_{\tilde{K}}$ planes in Fig. 4. We again emphasize that these limits can be stronger or weaker because of their dependence on g_D, as seen in Fig. 4.

B. Production of new, light states at future e^+e^- colliders

As outlined in Sec. IV and shown in Fig. 3, many new possibilities open up for production of new, light, hidden particles in the Double Dark Portal model. We can classify the new physics processes into vector + scalar, radiative return, and massive diboson production topologies. For small ϵ and scalar mixing angle α, the leading processes are:

$e^+e^- \to \tilde{Z}H_0$: The usual Higgsstrahlung diagram is suppressed by $\cos^2\alpha$, with an additional contribution from intermediate $\tilde{K}^*$ that can interfere with $\tilde{Z}^*$ exchange.

$e^+e^- \to \tilde{Z}S$: This new process can be probed by the usual recoil mass method for well-reconstructed $\tilde{Z}$ decays, studying the entire recoil mass differential distribution.

$e^+e^- \to \tilde{K}S$: This exotic production process involves two non-standard objects, and is dominantly produced via $\tilde{K}^*$, with a rate proportional to $\epsilon^2\cos^2\alpha$. Since $\tilde{K}$ and S dominantly decay to dark matter, though, we would require an additional photon or a visible decay of $\tilde{K}$ or S in order to tag the event.

$e^+e^- \to \tilde{A}\tilde{K}$: The radiative return process produces $\tilde{K}$ in association with a hard photon $\tilde{A} \sim \gamma$, giving direct sensitivity to ϵ. We remark that the $\tilde{K} \to \ell^+\ell^-$ decay has been studied for $m_{\tilde{K}}$ between 10 GeV to 240 GeV at an $\sqrt{s} = 250$ GeV machine with 10 ab^{-1} [9], giving $\epsilon \lesssim 5 \times 10^{-4}$, if the decay $\tilde{K} \to \ell^+\ell^-$ is assumed dominant.

$e^+e^- \to \tilde{Z}\tilde{K}$**:** The massive diboson pair production process also provides direct sensitivity to ϵ, but measuring the rate precisely will pay leptonic branching fractions of the $\tilde{Z}$.

$e^+e^- \to H_0\tilde{K}$**:** This very interesting scenario can be probed by using the 125 GeV SM-like Higgs as a recoil candidate for the $\tilde{K}$ heavy vector. The total rate gives sensitivity to both ϵ and α and highlights the power of considering the SM-like Higgs as a signal probe for new physics.

Having identified the main production modes for the $\tilde{K}$ and S states, we can match them to decay topologies illustrated in the bottom row of Fig. 3. We also include the underexplored decay $H_0 \to \tilde{K}\tilde{Z}$, which gives an exotic decay of the SM-like Higgs into the SM-like $\tilde{Z}$ boson and the hidden photon $\tilde{K}$ sensitive to ϵ. As mentioned in Sec. III, we focus on $S \to \tilde{K}\tilde{K} \to 4\chi$ and $\tilde{K} \to \bar{\chi}\chi$, and thus the dark portal couplings must be tested by recoil mass techniques or mono-energetic photon spectra searches. We also demonstrate the importance of these missing energy searches by explicitly considering leptonic decays of $\tilde{K}$ in the $\tilde{Z}\tilde{K}$ and $\gamma\tilde{K}$ processes as well as the fully inclusive recoil mass distribution targeting $\gamma\tilde{K}$ production.

Since the workhorse SM Higgsstrahlung process has been studied extensively [2–4], we use these previous results to recast the sensitivity for ϵ and α. We also ignore the $\tilde{K}S$ production mode, since the dominant signature has nothing visible to tag the event. The $H_0\tilde{K}$ process is interesting to consider for future work, but it requires optimizing the H_0 decay channel to gain maximum sensitivity to the recoil mass of the rest of the event.

This leaves the $\tilde{Z}H_0$, $\tilde{Z}S$, $\gamma\tilde{K}$ and $\tilde{Z}\tilde{K}$ processes as new opportunities to revisit or study. We simulate each process using MadGraph5 v2.4.3 [86], Pythia v6.4 [87] for showering and hadronization, and Delphes v3.2 [88] for detector simulation. Detector performance parameters were taken from the preliminary validated CEPC Delphes card [89]. Backgrounds for each process are generated including up to one additional photon to account for initial state and final state radiation effects. Events are required to pass preselection cuts of $|\eta| < 2.3$ for all visible particles, while photons and charged leptons must have $E > 5$ GeV, jets must have $E > 10$ GeV, and missing transverse energy must satisfy $\not{E} > 10$ GeV. Our analysis is insensitive to the dark matter mass as long as $\tilde{K}$ and S give missing energy signatures.

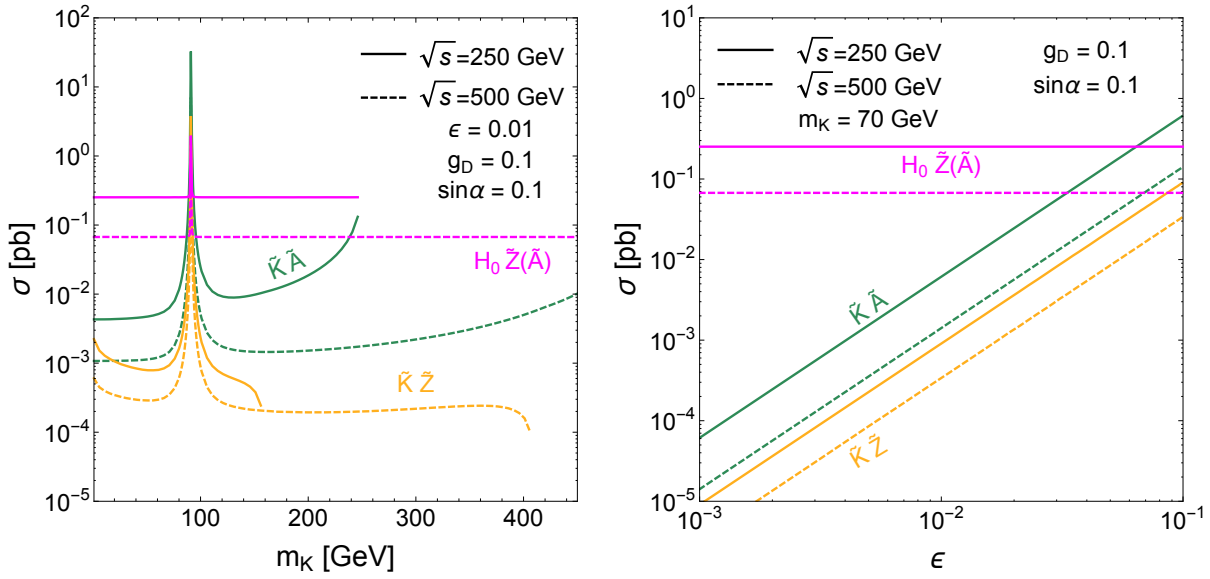

FIG. 5. Cross sections for $\tilde{Z}H_0$, $\tilde{A}\tilde{K}$, and $\tilde{Z}\tilde{K}$ processes as a function of (left panel) m_K or (right panel) ϵ. Solid lines correspond to e^+e^- machines operating at $\sqrt{s} = 250$ GeV with unpolarized beams, while dashed lines correspond to $\sqrt{s} = 500$ GeV. The mass of $\tilde{K}$ is derived from m_K using Eq. (11).

C. Testing ϵ and $\sin\alpha$ with new particle production

1. $\tilde{Z}\tilde{K}$ production

The cross section for $\tilde{Z}\tilde{K}$ production is shown in Fig. 5 for various choices of m_K and ϵ. We see that $\tilde{Z}\tilde{K}$ production grows with ϵ^2, as expected. We consider both $\tilde{K} \to \ell^+\ell^-$ and $\tilde{K} \to \bar{\chi}\chi$ decays, for $\ell = e$ or μ, where the missing energy branching ratio dominates by g_D^2/ϵ^2. We also study $\tilde{Z} \to \ell^+\ell^-$ with the SM branching fraction of 6.8% [90]. We show the background cross sections for the corresponding $2\ell 2\nu$ and 4ℓ final states after the preselection cuts described in Subsec. V B in Table I. The $2\ell 2\nu$ background includes a combination of $Z\nu\nu$, ZZ and W^+W^- processes, while the 4ℓ background is mainly attributed to $ZZ/Z\gamma^*$ production.

For the $2\ell + \not{E}$ final state, we require a Z-candidate with $|m_{\ell\ell} - m_Z| < 10$ GeV and then look for a peak in the recoil mass distribution, see Eq. (31). For the 4ℓ final state, we identify the Z-candidate from the opposite-sign, same-flavor dilepton pair whose invariant mass is closest to the Z mass and then study the invariant mass distribution of the remaining dilepton pair. The $\tilde{K}$ signal is tested for each signal mass point in the corresponding mass distributions, and we draw 95% C.L. exclusion regions for each channel in the ϵ vs. m_K plane for an integrated luminosity $L = 5$ ab^{-1} in Fig. 6. The relative weight between the $2\ell 2\chi$ and 4ℓ final states is fixed by choosing

Parameter	Signal process		Background (pb)		Signal region
ϵ	$\tilde{Z}\tilde{K}$	$\tilde{Z} \to \bar{\ell}\ell$, $\tilde{K} \to \bar{\chi}\chi$	$\bar{\ell}\ell\bar{\nu}\nu$	0.929 (250 GeV)	$N_\ell \geq 2$, $\lvert m_{\ell\ell} - m_Z \rvert < 10$ GeV,
				0.545 (500 GeV)	and $\lvert m_{\rm recoil} - m_{\tilde{K}} \rvert < 2.5$ GeV
		$\tilde{Z} \to \bar{\ell}\ell$, $\tilde{K} \to \bar{\ell}\ell$	$\bar{\ell}\ell\bar{\ell}\ell$	0.055 (250 GeV)	$N_\ell \geq 4$, $\lvert m_{\ell\ell} - m_Z \rvert < 10$ GeV,
				0.023 (500 GeV)	and $\lvert m_{\ell\ell} - m_{\tilde{K}} \rvert < 2.5$ GeV
	$\tilde{A}\tilde{K}$	$\tilde{K}$ inclusive decay	$\gamma\bar{f}f$	23.14 (250 GeV)	$N_\gamma \geq 1$, and
				8.88 (250 GeV)	$\lvert E_\gamma - (\frac{\sqrt{s}}{2} - \frac{m_{\tilde{K}}^2}{2\sqrt{s}}) \rvert < 2.5$ GeV
		$\tilde{K} \to \bar{\ell}\ell$	$\gamma\bar{\ell}\ell$	12.67 (250 GeV)	$N_\gamma \geq 1$, $N_\ell \geq 2$, $\lvert E_\gamma - (\frac{\sqrt{s}}{2} - \frac{m_{\tilde{K}}^2}{2\sqrt{s}}) \rvert < 2.5$ GeV,
				4.38 (500 GeV)	and $\lvert m_{\ell\ell} - m_{\tilde{K}} \rvert < 5$ GeV
		$\tilde{K} \to \bar{\chi}\chi$	$\gamma\bar{\nu}\nu$	3.45 (250 GeV)	$N_\gamma \geq 1$, $\lvert E_\gamma - (\frac{\sqrt{s}}{2} - \frac{m_{\tilde{K}}^2}{2\sqrt{s}}) \rvert < 2.5$ GeV,
				2.92 (500 GeV)	and $\not{E} > 50$ GeV
	$\tilde{Z}H_0$	$H_0 \to \tilde{K}\tilde{Z}$ with	$\bar{\ell}\bar{\ell}\ell\ell\bar{\nu}\nu$	1.8×10^{-5} (250 GeV)	$N_\ell \geq 4$, $\lvert m_{\ell\ell} - m_Z \rvert < 10$ GeV,
		$\tilde{K} \to \bar{\chi}\chi$, $\tilde{Z} \to \bar{\ell}\ell$		3.5×10^{-4} (500 GeV)	and $\lvert m_{\rm recoil} - m_{\tilde{K}} \rvert < 2.5$ GeV
$\sin\alpha$	$\tilde{Z}S$	$\tilde{Z} \to \bar{\ell}\ell$	$\bar{\ell}\ell\bar{\nu}\nu$	0.87 (250 GeV)	$N_\ell \geq 2$, $\lvert m_{\ell\ell} - m_Z \rvert < 10$ GeV,
		$S \to \tilde{K}\tilde{K} \to 4\chi$		0.87 (250 GeV)	and $\lvert m_{\rm recoil} - m_S \rvert < 2.5$ GeV

TABLE I. Summary of the different vector + scalar and vector + vector production modes studied, along with the most salient cuts to identify the individual signals. All background processes include up to one additional photon to account for initial and final state radiation. Background rates are given for $\sqrt{s} = 250$ GeV or 500 GeV, and visible particles are required to satisfy preselection cuts given in the main text.

$g_D = e \approx 0.3$. We see that the fully visible 4ℓ final state performs worse than the $2\ell 2\nu$ signal selection, simply reflecting the dominant signal statistics in the missing energy channel.

2. $\tilde{A}\tilde{K}$ production

We study the radiative return process, $e^+e^- \to \tilde{A}\tilde{K}$, for $\tilde{K} \to \bar{\chi}\chi$, $\ell^+\ell^-$, and inclusive decays. While each search will use the same observable, namely a monochromatic peak in the photon energy as in Eq. (30), the different contributions of SM backgrounds in each event selection will result in the best sensitivity for the $\tilde{K} \to \bar{\chi}\chi$ decay. Background rates and signal regions are shown in Table I. For the inclusive decay of $\tilde{K}$, the background $\gamma\bar{f}f$ is generated where f is a SM fermion, including neutrinos. As mentioned in Subsec. V B, the visible energy distribution is technically equivalent to the recoil mass distribution, and this equivalence is sharpest when the visible SM

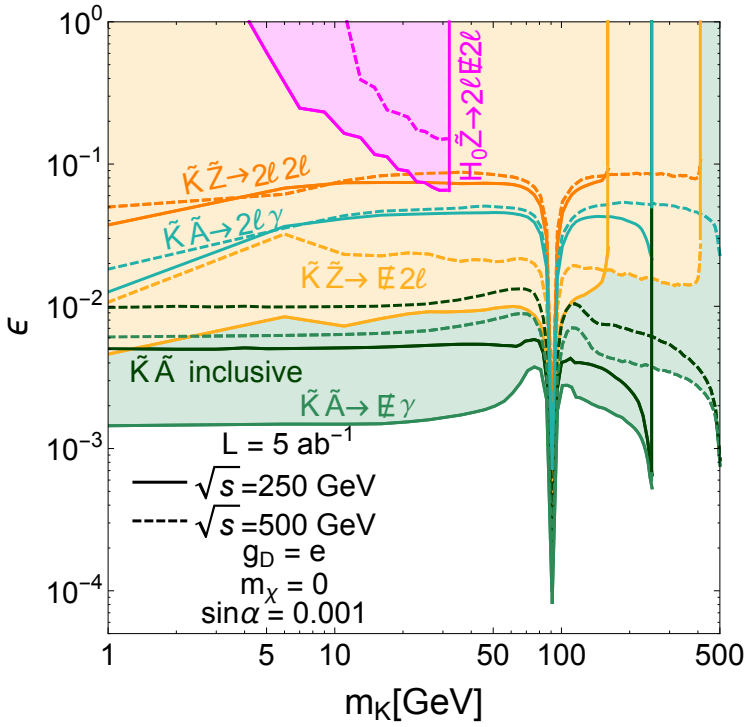

FIG. 6. Projected exclusion regions in the ϵ vs. m_K plane from multiple complementary searches of $\tilde{K}$ production. Solid lines enclose exclusion regions expected with $L = 5$ ab^{-1} of $\sqrt{s} = 250$ GeV e^+e^- machine data, while dashed lines correspond to a $\sqrt{s} = 500$ GeV machine. Note m_K is approximately the $m_{\tilde{K}}$ mass eigenvalue according to Eq. (11).

state is a single photon.

From the results in Fig. 6, we see that the most sensitive decay channel is $\tilde{K} \to \bar{\chi}\chi$, again reflecting the dominant statistics in this final state and the affordable reduction of SM backgrounds by the $\not{E}$ and mono-chromatic photon requirements.

The single photon in the background $\gamma\bar{\nu}\nu$ generally comes from initial state radiation and hence tends to be soft except when produced in the on-shell $\gamma\tilde{Z} \to \gamma\bar{\nu}\nu$ process. As long as $m_K \neq m_{\tilde{Z}}$, however, the signal peak will not run overlap the background peak, and thus we have a flat sensitivity to ϵ when $m_K < m_{\tilde{Z}}$. There are two spikes in ϵ exclusion sensitivity. The first is for $m_K \sim m_{\tilde{Z}}$, when the production cross section is greatly enhanced due to maximal $\tilde{K} - \tilde{Z}$ mixing, and the second is for $m_K \sim \sqrt{s}$, when the production is enhanced by soft, infrared divergent photon emission. Note the exclusion can only reach $m_K \sim \sqrt{s} - 5$ GeV because of the preselection cut on the photon energy.

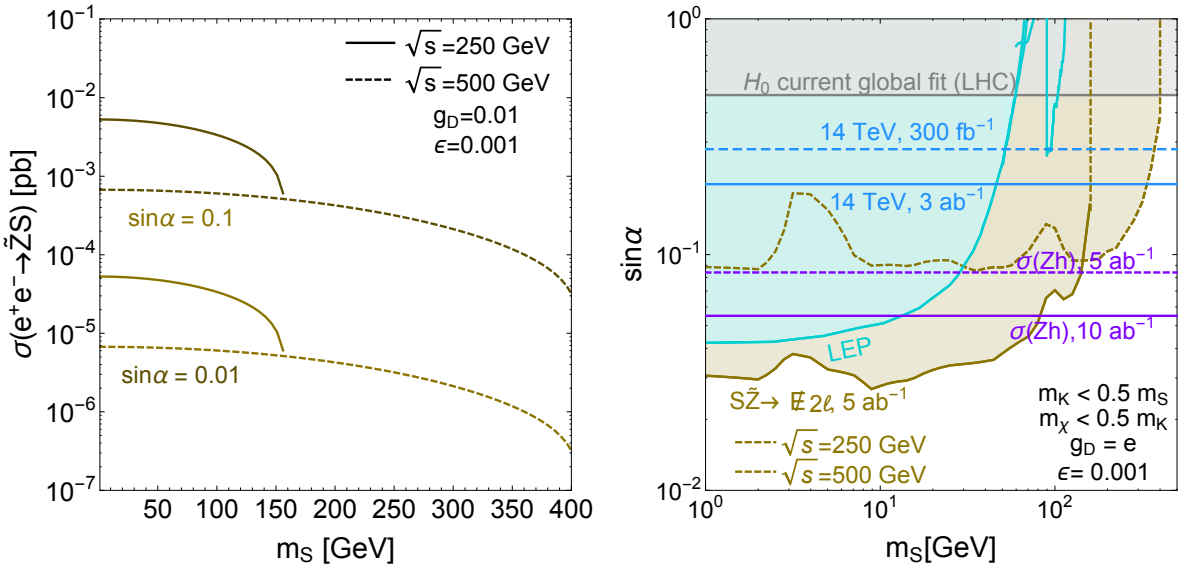

FIG. 7. (Left panel) Cross section rates for the $e^+e^- \to \tilde{Z}S$ process at $\sqrt{s} = 250$ GeV and 500 GeV as a function of m_S, with $\sin\alpha = 0.1$ and 0.01. (Right panel) Exclusion reach from the $\tilde{Z}S$, $\tilde{Z} \to \ell^+\ell^-$ search in the recoil mass distribution for invisible S decays in the $\sin\alpha$ vs. m_S plane using 5 ab^{-1} of e^+e^- data at $\sqrt{s} = 250$ GeV or 500 GeV. We also show comparisons to the current fit, $\sin\alpha < 0.47$ [60], future LHC projections of 0.28 (0.20) using 300 fb^{-1} (3 ab^{-1}) luminosity [1], and precision $\sigma(Zh)$ measurements constraining 0.084 (0.055) using 5 ab^{-1} (10 ab^{-1}) [3, 4, 85]. We plot the excluded region from LEP searches for invisible low mass Higgs in ZS channel in cyan [16–19].

3. $\tilde{Z}H_0$, $H_0 \to \tilde{K}\tilde{Z}$ *exotic decay*

The next process we consider is the exotic Higgs decay, $H_0 \to \tilde{K}\tilde{Z}$, with $\tilde{K} \to \bar{\chi}\chi$ and $\tilde{Z} \to \ell^+\ell^-$. This Higgs exotic decay partial width, from Eq. (35), is proportional to $\epsilon^2\cos^2\alpha$, as long as $m_{\tilde{K}} \lesssim 34$ GeV and $\sin\alpha$ is neglected. The signal process thus has 2 Z candidates balancing an invisible $\tilde{K}$ particle, which we identify from the peak in the recoil mass distribution. Our event selection cuts, summarized in Table I, require two pairs of opposite sign and same flavor lepton with invariant masses in a window around $m_{\tilde{Z}}$, and the recoil mass from the four visible charged leptons should be in a window around the test variable $m_{\tilde{K}}$. The resulting sensitivity, as seen in Fig. 6, is not competitive with the other $\tilde{K}$ production processes, given the limited Higgs production statistics and the suppression of the small leptomic decay branching ratio of $\tilde{Z}$. We remark that this decay can also be probed via $H_0 \to$ invisible searches using the SM rate for $Z \to \bar{\nu}\nu$, which was discussed in Subsec. IV C.

4. $\tilde{Z}S$ production

Lastly, we can also probe the scalar mixing angle $\sin\alpha$ in $\tilde{Z}S$ production. This search is exactly analogous to the previous search at LEP-II for a purely invisible decaying Higgs [16], where the visible $\tilde{Z} \to \ell^+\ell^-$ decay is used to construct the recoil mass distribution. The $\tilde{Z}S$ cross section is proportional to $\sin^2\alpha$ if we neglect ϵ, and $\sigma_{\tilde{Z}S}$ is shown in Fig. 7 for $\sin\alpha = 0.1$ and 0.01 at $\sqrt{s} = 250$ GeV and $\sqrt{s} = 500$ GeV. To maximize sensitivity to α, we study $\tilde{Z} \to \ell^+\ell^-$ and S decaying invisibly. The signal region is summarized in Table I and focuses on selecting a dilepton Z candidate and reconstructing the recoil mass distribution to identify the S peak. From this analysis, we find that $\sin\alpha = 0.03$ can be probed for light m_K using $L = 5$ ab^{-1} luminosity for $\sqrt{s} = 250$ GeV, as shown in Fig. 7. This result would significantly improve on the current global fit to Higgs data by ATLAS, which constrains $\sin\alpha < 0.47$ [60]. This sensitivity also exceeds the projected LHC reach of $\sin\alpha < 0.28$ (0.20) using 300 fb^{-1} (3 ab^{-1}) data and critical reductions in theoretical uncertainties [1]. We remark that improved sensivity can be obtained by varying the $\sqrt{s}$ of the collider to maximize the $\sigma(e^+e^- \to \tilde{Z}S)$ rate for the test S mass (see also Ref. [56]).

D. Summary

We summarize the sensitivity to ϵ in different channels at a future e^+e^- collider running at $\sqrt{s} = 250$ (500) GeV with $L = 5$ ab^{-1} in Fig. 8, and we compare the collider searches with constraints from direct detection and indirect detection experiments. In Fig. 8, the dark green shaded region is the exclusion limit from the strongest of the e^+e^- collider searches presented in Fig. 6. We also show the strongest limit from direct detection and indirect detection experiments from Fig. 1 and Fig. 2, as well as the contour satisfying the correct dark matter relic abundance measured by Planck [30]. While the constraints from dark matter detection experiments depend sensitively on the dark matter mass, the collider prospects are insensitive to the dark matter mass, as long as the decay to χ is kinematically allowed and $g_D \gg \epsilon$. We note that for m_K around $m_{\tilde{Z}}$, the best limit comes from the inclusive $\tilde{A}\tilde{K}$ search, which is insensitive to g_D, while for m_K larger or smaller than $m_{\tilde{Z}}$, the best sensitivity comes from the monochromatic photon search with $\not{E}$.

On the other hand, the indirect detection sensitivity and the relic abundance contour both change significantly with dark matter mass. When $m_\chi = 0.495 m_K$, the dark matter resonantly annihilates, improving the reach for indirect searches and dramatically lowering the required ϵ to satisfy the relic density measurement. During thermal freeze-out, the finite temperature of the

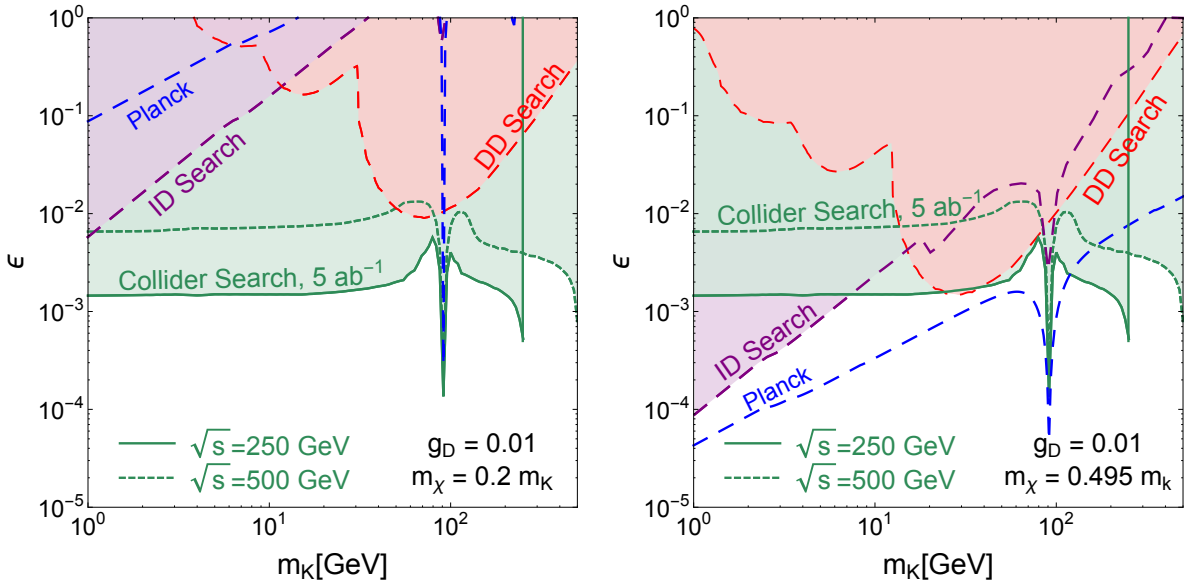

FIG. 8. Combined results of direct detection (red), indirect detection (purple), and collider searches (dark green) in the ϵ vs. m_K plane. We choose $g_D = 0.01$, $m_\chi = 0.2m_K$ (left panel) and $m_\chi = 0.495m_K$ (right panel). We also show the contours when χ satisfies the relic density measurement by the Planck collaboration [30] as blue dashed lines. The collider constraint is adapted from Fig. 6, taking into account the changes in the $\tilde{K}$ branching fractions.

χ velocity distribution gives a strong boost to the annihilation cross section, and thus only very small ϵ is needed. For $m_\chi = 0.2m_K$, however, the limits from indirect detection exclude the relic abundance contour, and the parameter space is instead characterized by an overabundance of the dark matter relic density. For this region to satisfy the Planck bound, additional mediators or new dark matter dynamics controlling the freeze-out behavior are needed. Direct detection experiments also lose sensivity to dark matter signals for light m_χ, since the nuclear recoil spectrum is too soft to pass the fiducial energy threshold. In addition, the decreasing sensivity for heavy m_χ comes from the fall off in the scattering cross section scaling as $\mu_{\chi p}^2/m_{\tilde{K}}^2$, see Eq. (28).

We also emphasize that the collider constraint is not sensitive to varying g_D as long as $g_D \gg \epsilon$, which ensures the invisible decay of $\tilde{K}$ dominates. Hence, the collider constraints from Fig. 6 and Fig. 8 are essentially unchanged, since changing g_D from e to 0.01 does not significantly change the invisible branching fraction, except for the tradeoff between inclusive $\tilde{K}$ decays and invisible $\tilde{K}$ decays around $m_K \approx m_{\tilde{Z}}$. On the other hand, the direct detection and indirect detection rates scale with g_D^2, and thus collider searches will have better sensitivity for small g_D.

From Fig. 8, we see that the prospective collider limits, corresponding to the radiative return process $e^+e^- \to \tilde{A}\tilde{K}$, are expected to overtake the current bounds from direct detection and indirect

detection experiments. In the case where dark matter mass is light, $m_\chi = 0.2 m_K$, the collider limits are typically at least one order of magnitude stronger than the current limits, especially in the high mass region, and hence out of the reach of next generation 1-ton scale direct detection experiments. For dark matter close to half the mediator mass, $m_\chi = 0.495 m_K$, the thermal relic abundance measured by Planck [30] offers an attractive target parameter space for experimental probes. The projected e^+e^- sensitivity exceeds the current experimental sensitivity around $m_K \sim 10$ GeV and $m_K > 100$ GeV, and while improvements in the dark matter experiments will also challenge the open parameter space for $m_K \sim 10$ GeV, the striking sensitivity of e^+e^- radiative return processes for $m_K > 100$ GeV is expected to be unmatched. Thus, results from a future e^+e^- collider will both complement and supercede the reach from dark matter searches, stemming from its ability to produce directly the mediators of dark matter interactions.

VI. CONCLUSION

We have presented a comprehensive discussion of the phenomenology of the Double Dark Portal model, which addresses the simultaneous possibility of a kinetic mixing ϵ parameter with a scalar Higgs portal λ. We emphasize that these Lagrangian parameters are generic in any $U(1)$ extension of the SM when the additional gauge symmetry is Higgsed. An additional motivation for considering such a $U(1)$ extension is the fact that such a symmetry readily stabilizes the lightest dark sector fermion χ, making this model a natural framework to study possible dark matter interactions in tandem with updated precision Z and Higgs constraints anticipated at future colliders. This study also demonstrates the ability of a future e^+e^- machine to produce new particles, which are not probed with the current dark matter and LHC experiments.

We work out the interactions in the mass eigenstate basis of neutral vector bosons and Higgses. The direct detection limits for this model have been studied, along with indirect detection constraints from CMB measurements, gamma ray measurements, and $e^\pm$ measurements, where we have explored both the non-resonant and resonant dark matter parameter regions. For collider constraints, we discussed the existing bounds from by electroweak precision and Z-pole observables, Higgs measurements, Drell-Yan measurements, and radiative return processes. Previous constraints have mostly focused on the visible decay, $\tilde{K} \to \ell^+\ell^-$, and leaving the prospects and sensitivity estimates for the invisible decay, $\tilde{K} \to \bar{\chi}\chi$ largely unexplored.

We studied both the Higgs bremsstrahlung and radiative return processes for a future e^+e^- collider, emphasizing that a future lepton collider not only has vital Higgs precision capabilities

but also new possibilities for producing light new particles, $\tilde{K}$ and S. Since both $\tilde{K}$ and S decays are dominantly invisible, the recoil mass method afforded by an e^+e^- machine is crucial. We also highlight that the recoil mass method can be simplified to a monochromatic photon study in the case that the new particle is produced in the radiative return process, which simplifies the search procedure and enhances the importance for upcoming calorimeters to have a precise, high-resolution energy determination for photons. The various Higgsstrahlung and radiative return processes we study are listed in Table I, and we obtain the best sensitivity on ϵ and $\sin\alpha$ from the radiative return process $\tilde{A}\tilde{K}$ and Higgsstrahlung process $\tilde{Z}S$, respectively.

In comparing ϵ prospects, we analyzed the future collider reach with direct detection, indirect detection and relic abundance sensitivities. The collider prospects are less affected by DM mass m_χ, and surpass the other experimental probes for small g_D. Since $\tilde{K}$ decays invisibly, the most relevant current constraints are from electroweak precision measurements and LHC mono-jet searches, but they are not as strong as the radiative return process $\tilde{A}\tilde{K}$ reach. Therefore, a future e^+e^- collider provides an important and complementary sensitivity test of the DDP model.

For $\sin\alpha$, the best constraints come from studying the singlet bremsstrahlung process $\tilde{Z}S$, the Higgs invisible decay rate, and precision measurements of SM Higgs production rates. We studied the $\tilde{Z}S$ process with S decaying invisibly for a future e^+e^- collider and estimated the sensitivity to be $\sin\alpha \sim 0.03$. This compares favorably with earlier LEP studies for light m_S, and readily provides leading sensitivity for heavy S. We also recasted bounds using the Higgs invisible decay channel, where the current LHC constraint is $\mathrm{BR}_{\mathrm{inv}} < 0.23$ [60, 61] and the future e^+e^- collider reach is $\mathrm{BR}_{\mathrm{inv}} < 0.005$ [3]. In the DDP model, these bounds simultaneously constrain the three exotic processes, $H_0 \to SS$, $H_0 \to \tilde{K}\tilde{K}$, and $H_0 \to \tilde{Z}\tilde{K}$ when $\tilde{Z}$ decays to neutrinos. While the constraints on $\sin\alpha$ can be strong, these limits also depend sensitively on g_D and are insignificant for small g_D. The future $\sigma(e^+e^- \to Zh)$ precision measurement readily constrains $\cos^2\alpha$, but this projection is weaker than the direct $\tilde{Z}S$ search.

In summary, the Double Dark Portal model predicts new dark sector particles, $\tilde{K}$, S, and χ, whose vector and scalar portal interactions with the Standard Model can be uniquely tested at a future e^+e^- collider. We explicitly propose and study radiative return and Higgsstrahlung processes to find the invisible decays of the $\tilde{K}$ and S mediators. An additional benefit of the e^+e^- search strategies discussed in this work is that, in the event of a discovery, the $\tilde{K}$ or S mass is immediately measured in the recoil mass distribution. Hence, a future e^+e^- collider not only has exciting prospects for determining the precise properties of the 125 GeV Higgs boson, but also has a unique and promising new physics program founded on the production of new, light, hidden

particles.

ACKNOWLEDGMENTS

This research is supported by the Cluster of Excellence Precision Physics, Fundamental Interactions and Structure of Matter (PRISMA-EXC 1098). FY would like to thank the hospitality of the CERN theory group while this work was being completed. The work of JL and XPW is also supported by the German Research Foundation (DFG) under Grants No. KO 4820/1–1, and No. FOR 2239, and from the European Research Council (ERC) under the European Union's Horizon 2020 research and innovation program (Grant No. 637506, "νDirections").

Appendix A: Two limiting cases for $\tilde{K}$, $\tilde{Z}$, and $\tilde{A}$ mixing

From Subsec. II A, we decompose the gauge eigenstate vectors into their mass eigenstate components according to

$$\begin{pmatrix} Z_{\mu,\,\mathrm{SM}} \\ A_{\mu,\,\mathrm{SM}} \\ K_\mu \end{pmatrix} = U_1 U_2 R_M \begin{pmatrix} \tilde{Z}_\mu \\ \tilde{A}_\mu \\ \tilde{K}_\mu \end{pmatrix} , \tag{A1}$$

where the expressions for U_1, U_2 and R_M have been given in Eq. (7), and Eq. (9), respectively. We will consider the two limiting cases, $m_K \to 0$ and $m_K \to m_{Z,\mathrm{SM}}$, and study the corresponding changes for the kinetic and mass mixing matrices.

For $m_K \to 0$, the gauge boson masses are

$$m_{\tilde{A}} = m_{\tilde{K}} = 0 , \tag{A2}$$

$$m_{\tilde{Z}}^2 = m_{Z,\,\mathrm{SM}}^2 \frac{1-\epsilon^2}{1-\epsilon^2 c_W^{-2}} \approx m_{Z,\,\mathrm{SM}}^2 \left(1+\epsilon^2 t_W^2\right) + \mathcal{O}(\epsilon^3) , \tag{A3}$$

and the field redefinition is

$$U_1 U_2 = \begin{pmatrix} \sqrt{\frac{1-\epsilon^2}{1-\epsilon^2 c_W^{-2}}} & 0 & 0 \\ -\frac{\epsilon^2 t_W}{\sqrt{(1-\epsilon^2)(1-\epsilon^2 c_W^{-2})}} & 1 & \frac{\epsilon}{\sqrt{1-\epsilon^2}} \\ -\frac{\epsilon t_W}{\sqrt{(1-\epsilon^2)(1-\epsilon^2 c_W^{-2})}} & 0 & \frac{1}{\sqrt{1-\epsilon^2}} \end{pmatrix} \approx \begin{pmatrix} 1+\frac{1}{2}\epsilon^2 t_W^2 & 0 & 0 \\ -\epsilon^2 t_W & 1 & \epsilon \\ -\epsilon t_W & 0 & 1+\frac{1}{2}\epsilon^2 \end{pmatrix} + \mathcal{O}(\epsilon^3) . \tag{A4}$$

The Jacobi rotation R_M, from Eq. (9), is now ill-defined in the lower right two-by-two block, since $\tilde{A}$ and $\tilde{K}$ can be rotated into each other keeping both the kinetic terms and masses unchanged. This simply reflects the residual unbroken $U(1)_{\rm em} \times U(1)_D$ gauge symmetry. For $R_M = I_3$, the currents are

$$\begin{aligned}\mathcal{L} \supset\ & \tilde{Z}_\mu \left(g J_Z^\mu - g_D t_W \epsilon J_D^\mu + \frac{1}{2} g t_W^2 \epsilon^2 J_Z^\mu - e t_W \epsilon^2 J_{\rm em}^\mu \right) \\ & + \tilde{K}_\mu \left(g_D J_D^\mu + e\epsilon J_{\rm em}^\mu + \frac{1}{2} g_D \epsilon^2 J_D^\mu \right) \\ & + \tilde{A}_\mu e J_{\rm em}^\mu \ , \end{aligned} \tag{A5}$$

but under a unitary rotation U_X where $(\tilde{A}',\ \tilde{K}')^T = U_X(\tilde{A},\ \tilde{K})^T$, the dark matter χ and the SM fermions will generally have nonzero charges mediated by both $\tilde{A}'$ and $\tilde{K}'$, leading to photon and dark photon-mediated electric and dark millicharges.

For $m_K \to m_{Z,\,\rm SM}$, the masses of the three vector bosons are

$$m_{\tilde{A}} = 0, \quad m^2_{\tilde{K},\ \tilde{Z}} = m^2_{Z,\,\rm SM} \left(1 \mp \epsilon t_W + \frac{1}{2}\epsilon^2 \left(1 + 2 t_W^2 \right) \right) \ , \tag{A6}$$

and the field redefinition required, to $\mathcal{O}(\epsilon^2)$, is

$$U_1 U_2 R_M = \frac{1}{\sqrt{2}} \begin{pmatrix} 1 \mp \frac{\epsilon}{4}(t_W^{-1} - 2t_W) & 0 & \pm 1 + \frac{\epsilon}{4}(t_W^{-1} - 2t_W) \\ \mp\epsilon & \sqrt{2} & \epsilon \\ \mp 1 - \frac{\epsilon}{4}(t_W^{-1} + 2t_W) & 0 & 1 \mp \frac{\epsilon}{4}(t_W^{-1} + 2t_W) \end{pmatrix} \ , \tag{A7}$$

where the top and bottom signs correspond to $m_K \to m^{\mp}_{Z,\,\rm SM}$. We see that the mixing between Z_μ and K_μ is nearly maximal, 45°, while the discontinuous behavior for m_K below and above $m_{Z,\,\rm SM}$ reflects the level crossing in the mass eigenvalues. We remark that as long as $\epsilon \neq 0$, this maximal mixing feature remains, dictated by the structure of the symmetric mass matrix in Eq. (8). If $\epsilon = 0$ and $m_K = m_Z$, then the rotation matrix in Eq. (9) becomes ill-defined and the maximal mixing feature is lost.

Appendix B: Cancellation effect in multiple kinetic mixing terms

We observe that the $\tilde{Z}$ and $\tilde{K}$ mediated couplings in Eq. (15) show a cancellation effect when mediating DM interactions with SM fermions. This feature can be generalized to the situation with multiple $U(1)$ gauge groups with multiple kinetic mixing terms between each other. Explicitly, we

analyze the Lagrangian

$$\mathcal{L} \supset \frac{1}{4} V^T \mathcal{K} V + \frac{1}{2} V^T M^2 V \ , \tag{B1}$$

where $\mathcal{K}_{ab} = \delta_{ab} + \mathcal{O}(\epsilon)(1-\delta_{ab})$ is the kinetic mixing matrix and M^2 is the diagonal mass matrix, with a, b as indices. Then, we define the field redefinition matrix U such that $U^T \mathcal{K} U = \mathbb{I}$, which also gives $\tilde{M}^2 = U^T M^2 U$ as the mass matrix corresponding to the mass eigenstates, $\tilde{V} = U^{-1} V$. Moreover, the gauge currents now become

$$\mathcal{L} \supset g_i V_\mu^i J_i^\mu = g_i U_{ik} \tilde{V}_{k,\mu} J_i^\mu, \tag{B2}$$

in the mass basis. As a result, scattering rates between two currents J_a and J_b (which represent the corresponding fermion bilinears) are schematically

$$\begin{aligned} \mathcal{M} &\propto (g_a J_a^\mu) \otimes (g_b J_b^\nu) \left[U_{ak} U_{bk} \frac{g_{\mu\nu} - q_\mu q_\nu / m_{\tilde{V}_k}^2}{Q^2 - m_{\tilde{V}_k}^2} \right] \\ &\sim (g_a J_a^\mu) \otimes (g_b J_b^\nu) \left[U_{ak} (U^T)_{kb} \left(\frac{-g_{\mu\nu}}{m_{\tilde{V}_k}^2} + g_{\mu\nu}\, \mathcal{O}(\frac{Q^2}{m_{\tilde{V}_k}^4}) \right) \right] \ . \end{aligned} \tag{B3}$$

The $-g_{\mu\nu}/m_{\tilde{V}_k}^2$ term in the parentheses, however, vanishes, when including the sum over $U_{ak}(U^T)_{kb}$, because these transformations are controlled by the diagonalization requirement of the two mass matrices, specifically $U \tilde{M}^{-2} U^T = M^{-2}$. The leading contribution in the amplitude is then proportional to $\epsilon Q^2 / m_{\tilde{V}}^2$.

Appendix C: Annihilation cross sections

In this section, we present the annihilation cross sections for the processes $\bar{\chi}\chi \to \bar{f} f$, W^+W^-, where f is a SM fermion. We focus on the case with $m_\chi < m_{\tilde{K}}$, since otherwise the direct annihilation of dark matter to dark vectors $\tilde{K}\tilde{K}$ opens up and does not depend on ϵ. In this setup, the annihilation cross section is proportional to $g_D^2 \epsilon^2$. The diagrams include s-channel $\tilde{K}$ and $\tilde{Z}$ exchange. The annihilation cross sections before thermal averaging are

$$\begin{aligned} \sigma v \left(\bar{\chi}\chi \to \ell^+\ell^-\right) = & \frac{e^2 \epsilon^2 g_D^2 \sqrt{s - 4m_\ell^2} \left(2m_\chi^2 + s\right)}{48\pi s^{3/2} c_W^4 \left(m_{\tilde{Z}}^2 - m_{\tilde{K}}^2\right)^2 \left(m_{\tilde{Z}}^2 \Gamma_{\tilde{Z}}^2 + \left(s - m_{\tilde{Z}}^2\right)^2\right) \left(m_{\tilde{K}}^2 \Gamma_{\tilde{K}}^2 + \left(s - m_{\tilde{K}}^2\right)^2\right)} \\ & \times \Big[\left(5s + 7m_\ell^2\right) \left(s^2 (m_{\tilde{Z}}^2 - m_{\tilde{K}}^2)^2 + m_{\tilde{Z}}^2 m_{\tilde{K}}^2 (m_{\tilde{K}} \Gamma_{\tilde{Z}} - m_{\tilde{Z}} \Gamma_{\tilde{K}})^2 \right) \\ & - 12 c_W^2 (s + 2m_\ell^2) m_{\tilde{Z}}^2 \left(s (m_{\tilde{Z}}^2 - m_{\tilde{K}}^2)^2 + m_{\tilde{Z}} m_{\tilde{K}} (-m_{\tilde{K}} \Gamma_{\tilde{Z}} + m_{\tilde{Z}} \Gamma_{\tilde{K}})(-m_{\tilde{Z}} \Gamma_{\tilde{Z}} + m_{\tilde{K}} \Gamma_{\tilde{K}}) \right) \\ & + 8 c_W^2 (s + 2m_\ell^2) m_{\tilde{Z}}^4 \left(m_{\tilde{K}}^4 + m_{\tilde{Z}}^2 (m_{\tilde{Z}}^2 + \Gamma_{\tilde{Z}}^2) - 2 m_{\tilde{Z}} m_{\tilde{K}} \Gamma_{\tilde{Z}} \Gamma_{\tilde{K}} + m_{\tilde{K}}^2 (-2m_{\tilde{Z}}^2 + \Gamma_{\tilde{K}}^2) \right) \Big] \ , \end{aligned} \tag{C1}$$

$$\sigma v\left(\bar{\chi}\chi \to \bar{u}u\right) = \frac{e^2\epsilon^2 g_D^2 \sqrt{s-4m_u^2}\left(2m_\chi^2+s\right)}{144\pi s^{3/2} c_W^4 \left(m_{\tilde{Z}}^2 - m_{\tilde{K}}^2\right)^2 \left(m_{\tilde{Z}}^2\Gamma_{\tilde{Z}}^2 + \left(s-m_{\tilde{Z}}^2\right)^2\right)\left(m_{\tilde{K}}^2\Gamma_{\tilde{K}}^2 + \left(s-m_{\tilde{K}}^2\right)^2\right)}$$
$$\times \Big[\left(17s+7m_u^2\right)\left(s^2(m_{\tilde{Z}}^2-m_{\tilde{K}}^2)^2 + m_{\tilde{Z}}^2 m_{\tilde{K}}^2 (m_{\tilde{K}}\Gamma_{\tilde{Z}} - m_{\tilde{Z}}\Gamma_{\tilde{K}})^2\right)$$
$$- 40c_W^2(s+2m_u^2)m_{\tilde{Z}}^2\left(s(m_{\tilde{Z}}^2-m_{\tilde{K}}^2)^2 + m_{\tilde{Z}}m_{\tilde{K}}(-m_{\tilde{K}}\Gamma_{\tilde{Z}} + m_{\tilde{Z}}\Gamma_{\tilde{K}})(-m_{\tilde{Z}}\Gamma_{\tilde{Z}} + m_{\tilde{K}}\Gamma_{\tilde{K}})\right)$$
$$+ 32c_W^4(s+2m_u^2)m_{\tilde{Z}}^4\left(m_{\tilde{K}}^4 + m_{\tilde{Z}}^2(m_{\tilde{Z}}^2+\Gamma_{\tilde{Z}}^2) - 2m_{\tilde{Z}}m_{\tilde{K}}\Gamma_{\tilde{Z}}\Gamma_{\tilde{K}} + m_{\tilde{K}}^2(-2m_{\tilde{Z}}^2+\Gamma_{\tilde{K}}^2)\right)\Big] \ , \quad \text{(C2)}$$

$$\sigma v\left(\bar{\chi}\chi \to \bar{d}d\right) = \frac{e^2\epsilon^2 g_D^2 \sqrt{s-4m_d^2}\left(2m_\chi^2+s\right)}{144\pi s^{3/2} c_W^4 \left(m_{\tilde{Z}}^2 - m_{\tilde{K}}^2\right)^2 \left(m_{\tilde{Z}}^2\Gamma_{\tilde{Z}}^2 + \left(s-m_{\tilde{Z}}^2\right)^2\right)\left(m_{\tilde{K}}^2\Gamma_{\tilde{K}}^2 + \left(s-m_{\tilde{K}}^2\right)^2\right)}$$
$$\times \Big[\left(5s-17m_d^2\right)\left(s^2(m_{\tilde{Z}}^2-m_{\tilde{K}}^2)^2 + m_{\tilde{Z}}^2 m_{\tilde{K}}^2 (m_{\tilde{K}}\Gamma_{\tilde{Z}} - m_{\tilde{Z}}\Gamma_{\tilde{K}})^2\right)$$
$$- 4c_W^2(s+2m_d^2)m_{\tilde{Z}}^2\left(s(m_{\tilde{Z}}^2-m_{\tilde{K}}^2)^2 + m_{\tilde{Z}}m_{\tilde{K}}(-m_{\tilde{K}}\Gamma_{\tilde{Z}} + m_{\tilde{Z}}\Gamma_{\tilde{K}})(-m_{\tilde{Z}}\Gamma_{\tilde{Z}} + m_{\tilde{K}}\Gamma_{\tilde{K}})\right)$$
$$+ 8c_W^4(s+2m_d^2)m_{\tilde{Z}}^4\left(m_{\tilde{K}}^4 + m_{\tilde{Z}}^2(m_{\tilde{Z}}^2+\Gamma_{\tilde{Z}}^2) - 2m_{\tilde{Z}}m_{\tilde{K}}\Gamma_{\tilde{Z}}\Gamma_{\tilde{K}} + m_{\tilde{K}}^2(-2m_{\tilde{Z}}^2+\Gamma_{\tilde{K}}^2)\right)\Big] \ , \quad \text{(C3)}$$

$$\sigma v\left(\bar{\chi}\chi \to \bar{\nu}_\ell\nu_\ell\right) = \frac{e^2\epsilon^2 g_D^2\left(2m_\chi^2+s\right)\left(s^2(m_{\tilde{Z}}^2-m_{\tilde{K}}^2)^2 + m_{\tilde{Z}}^2 m_{\tilde{K}}^2 (m_{\tilde{K}}\Gamma_{\tilde{Z}} - m_{\tilde{Z}}\Gamma_{\tilde{K}})^2\right)}{48\pi c_W^4 \left(m_{\tilde{Z}}^2 - m_{\tilde{K}}^2\right)^2 \left(m_{\tilde{Z}}^2\Gamma_{\tilde{Z}}^2 + \left(s-m_{\tilde{Z}}^2\right)^2\right)\left(m_{\tilde{K}}^2\Gamma_{\tilde{K}}^2 + \left(s-m_{\tilde{K}}^2\right)^2\right)} \ , \quad \text{(C4)}$$

$$\sigma v\left(\bar{\chi}\chi \to W^+W^-\right) = \frac{e^2\epsilon^2 g_D^2\left(2m_\chi^2+s\right)\left(s-4m_W^2\right)^{3/2}\left(20sm_W^2+12m_W^4+s^2\right)}{96\pi s^{3/2} c_W^4 \left(m_{\tilde{Z}}^2 - m_{\tilde{K}}^2\right)^2 \left(m_{\tilde{Z}}^2\Gamma_{\tilde{Z}}^2 + \left(s-m_{\tilde{Z}}^2\right)^2\right)\left(m_{\tilde{K}}^2\Gamma_{\tilde{K}}^2 + \left(s-m_{\tilde{K}}^2\right)^2\right)}$$
$$\times \left(m_{\tilde{Z}}^4 + m_{\tilde{Z}}^2(-2m_{\tilde{K}}^2+\Gamma_{\tilde{Z}}^2) - 2m_{\tilde{Z}}m_{\tilde{K}}\Gamma_{\tilde{Z}}\Gamma_{\tilde{K}} + m_{\tilde{K}}^2(m_{\tilde{K}}^2+\Gamma_{\tilde{K}}^2)\right) \ , \quad \text{(C5)}$$

where s is the Mandelstam parameter for the center-of-mass energy squared.

---

[1] Sally Dawson *et al.*, "Working Group Report: Higgs Boson," in *Proceedings, 2013 Community Summer Study on the Future of U.S. Particle Physics: Snowmass on the Mississippi (CSS2013): Minneapolis, MN, USA, July 29-August 6, 2013* (2013) arXiv:1310.8361 [hep-ex].

[2] Gerald Aarons *et al.* (ILC), "International Linear Collider Reference Design Report Volume 2: Physics at the ILC," (2007), arXiv:0709.1893 [hep-ph].

[3] M. Bicer *et al.* (TLEP Design Study Working Group), "First Look at the Physics Case of TLEP," *Proceedings, Community Summer Study 2013: Snowmass on the Mississippi (CSS2013): Minneapolis, MN, USA, July 29-August 6, 2013*, JHEP **01**, 164 (2014), arXiv:1308.6176 [hep-ex].

[4] CEPC-SPPC Study Group, "CEPC-SPPC Preliminary Conceptual Design Report. 1. Physics and Detector," (2015).

[5] Peng-fei Yin, Jia Liu, and Shou-hua Zhu, "Detecting light leptophilic gauge boson at BESIII detector," Phys. Lett. **B679**, 362–368 (2009), arXiv:0904.4644 [hep-ph].

[6] Hai-Bo Li and Tao Luo, "Probing Dark force at BES-III/BEPCII," Phys. Lett. **B686**, 249–253 (2010), arXiv:0911.2067 [hep-ph].

[7] J. P. Lees *et al.* (BaBar), "Search for a Dark Photon in e^+e^- Collisions at BaBar," Phys. Rev. Lett. **113**, 201801 (2014), arXiv:1406.2980 [hep-ex].

[8] David Curtin, Rouven Essig, Stefania Gori, and Jessie Shelton, "Illuminating Dark Photons with High-Energy Colliders," JHEP **02**, 157 (2015), arXiv:1412.0018 [hep-ph].

[9] Marek Karliner, Matthew Low, Jonathan L. Rosner, and Lian-Tao Wang, "Radiative return capabilities of a high-energy, high-luminosity e^+e^- collider," Phys. Rev. **D92**, 035010 (2015), arXiv:1503.07209 [hep-ph].

[10] Vindhyawasini Prasad, Haibo Li, and Xinchou Lou, "Search for low-mass Higgs and dark photons at BESIII," in *7th International Workshop on Charm Physics (Charm 2015) Detroit, MI, USA, May 18-22, 2015* (2015) arXiv:1508.07659 [hep-ex].

[11] Yonit Hochberg, Eric Kuflik, and Hitoshi Murayama, "SIMP Spectroscopy," JHEP **05**, 090 (2016), arXiv:1512.07917 [hep-ph].

[12] E. Won *et al.* (Belle), "Search for a dark vector gauge boson decaying to $\pi^+\pi^-$ using $\eta \to \pi^+\pi^-\gamma$ decays," Phys. Rev. **D94**, 092006 (2016), arXiv:1609.05599 [hep-ex].

[13] Min He, Xiao-Gang He, and Cheng-Kai Huang, "Dark Photon Search at A Circular e^+e^- Collider," (2017), arXiv:1701.08614 [hep-ph].

[14] Takeshi Araki, Shihori Hoshino, Toshihiko Ota, Joe Sato, and Takashi Shimomura, "Cornering the $L_\mu - L_\tau$ gauge boson at Belle-II," (2017), arXiv:1702.01497 [hep-ph].

[15] Sanjoy Biswas, Emidio Gabrielli, Matti Heikinheimo, and Barbara Mele, "Dark-photon searches via ZH production at e^+e^- colliders," (2017), arXiv:1703.00402 [hep-ph].

[16] M. Acciarri *et al.* (L3), "Search for neutral Higgs boson production through the process e+ e- → Z* H0," Phys. Lett. **B385**, 454–470 (1996).

[17] M. Acciarri *et al.* (L3), "Missing mass spectra in hadronic events from e+ e- collisions at s**(1/2) = 161-GeV - 172-GeV and limits on invisible Higgs decay," Phys. Lett. **B418**, 389–398 (1998).

[18] P. Abreu *et al.* (DELPHI), "A Search for invisible Higgs bosons produced in e+ e- interactions at LEP-2 energies," Phys. Lett. **B459**, 367–381 (1999).

[19] "Searches for invisible Higgs bosons: Preliminary combined results using LEP data collected at energies up to 209-GeV," in *Lepton and photon interactions at high energies. Proceedings, 20th International Symposium, LP 2001, Rome, Italy, July 23-28, 2001* (2001) arXiv:hep-ex/0107032 [hep-ex].

[20] S. Schael *et al.* (DELPHI, OPAL, ALEPH, LEP Working Group for Higgs Boson Searches, L3), "Search for neutral MSSM Higgs bosons at LEP," Eur. Phys. J. **C47**, 547–587 (2006), arXiv:hep-ex/0602042 [hep-ex].

[21] Thomas Flacke, Claudia Frugiuele, Elina Fuchs, Rick S. Gupta, and Gilad Perez, "Phenomenology of relaxion-Higgs mixing," (2016), arXiv:1610.02025 [hep-ph].

[22] I. Jaegle (Belle), "Search for the dark photon and the dark Higgs boson at Belle," Phys. Rev. Lett. **114**, 211801 (2015), arXiv:1502.00084 [hep-ex].

[23] Sanjoy Biswas, Emidio Gabrielli, Matti Heikinheimo, and Barbara Mele, "Higgs-boson production in association with a dark photon in e+e- collisions," JHEP **06**, 102 (2015), arXiv:1503.05836 [hep-ph].

[24] Andrei Angelescu, Grégory Moreau, and François Richard, "Scalar Production in Association with a Z Boson at LHC and ILC: the Mixed Higgs-Radion Case of Warped Models," (2017), arXiv:1702.03984 [hep-ph].

[25] Jim Alexander *et al.*, "Dark Sectors 2016 Workshop: Community Report," (2016) arXiv:1608.08632 [hep-ph].

[26] R. Agnese *et al.* (SuperCDMS), "New Results from the Search for Low-Mass Weakly Interacting Massive Particles with the CDMS Low Ionization Threshold Experiment," Phys. Rev. Lett. **116**, 071301 (2016), arXiv:1509.02448 [astro-ph.CO].

[27] G. Angloher *et al.* (CRESST), "Results on light dark matter particles with a low-threshold CRESST-II detector," Eur. Phys. J. **C76**, 25 (2016), arXiv:1509.01515 [astro-ph.CO].

[28] Andi Tan *et al.* (PandaX-II), "Dark Matter Results from First 98.7 Days of Data from the PandaX-II Experiment," Phys. Rev. Lett. **117**, 121303 (2016), arXiv:1607.07400 [hep-ex].

[29] D. S. Akerib *et al.* (LUX), "Results from a search for dark matter in the complete LUX exposure," Phys. Rev. Lett. **118**, 021303 (2017), arXiv:1608.07648 [astro-ph.CO].

[30] P. A. R. Ade *et al.* (Planck), "Planck 2015 results. XIII. Cosmological parameters," (2015), arXiv:1502.01589 [astro-ph.CO].

[31] M. Ackermann *et al.* (Fermi-LAT), "Searching for Dark Matter Annihilation from MilkyÂ Way Dwarf Spheroidal Galaxies with Six Years of Fermi Large Area Telescope Data," Phys. Rev. Lett. **115**, 231301 (2015), arXiv:1503.02641 [astro-ph.HE].

[32] M. L. Ahnen *et al.* (Fermi-LAT, MAGIC), "Limits to dark matter annihilation cross-section from a combined analysis of MAGIC and Fermi-LAT observations of dwarf satellite galaxies," JCAP **1602**, 039 (2016), arXiv:1601.06590 [astro-ph.HE].

[33] Andrea Massari, Eder Izaguirre, Rouven Essig, Andrea Albert, Elliott Bloom, and German Arturo Gomez-Vargas, "Strong Optimized Conservative $Fermi$-LAT Constraints on Dark Matter Models from the Inclusive Photon Spectrum," Phys. Rev. **D91**, 083539 (2015), arXiv:1503.07169 [hep-ph].

[34] M. Aguilar *et al.* (AMS), "Electron and Positron Fluxes in Primary Cosmic Rays Measured with the Alpha Magnetic Spectrometer on the International Space Station," Phys. Rev. Lett. **113**, 121102 (2014).

[35] Morad Aaboud *et al.* (ATLAS), "Search for new phenomena in final states with an energetic jet and large missing transverse momentum in pp collisions at $\sqrt{s} = 13$ TeV using the ATLAS detector," Phys. Rev. **D94**, 032005 (2016), arXiv:1604.07773 [hep-ex].

[36] Albert M Sirunyan *et al.* (CMS), "Search for dark matter produced with an energetic jet or a hadronically decaying W or Z boson at $\sqrt{s} = 13$ TeV," (2017), arXiv:1703.01651 [hep-ex].

[37] Jia Liu, Neal Weiner, and Wei Xue, "Signals of a Light Dark Force in the Galactic Center," JHEP **08**, 050 (2015), arXiv:1412.1485 [hep-ph].

[38] Kim Griest and David Seckel, "Three exceptions in the calculation of relic abundances," Phys. Rev. **D43**, 3191–3203 (1991).

[39] Michael J. Baker *et al.*, "The Coannihilation Codex," JHEP **12**, 120 (2015), arXiv:1510.03434 [hep-ph].

[40] Malte Buschmann, Sonia El Hedri, Anna Kaminska, Jia Liu, Maikel de Vries, Xiao-Ping Wang, Felix Yu, and Jose Zurita, "Hunting for dark matter coannihilation by mixing dijet resonances and missing transverse energy," JHEP **09**, 033 (2016), arXiv:1605.08056 [hep-ph].

[41] Alexandre Alves, Giorgio Arcadi, Yann Mambrini, Stefano Profumo, and Farinaldo S. Queiroz, "Augury of Darkness: The Low-Mass Dark Z' Portal," (2016), arXiv:1612.07282 [hep-ph].

[42] Rouven Essig *et al.*, "Working Group Report: New Light Weakly Coupled Particles," in *Proceedings, 2013 Community Summer Study on the Future of U.S. Particle Physics: Snowmass on the Mississippi (CSS2013): Minneapolis, MN, USA, July 29-August 6, 2013* (2013) arXiv:1311.0029 [hep-ph].

[43] Henri Ruegg and Marti Ruiz-Altaba, "The Stueckelberg field," Int. J. Mod. Phys. **A19**, 3265–3348 (2004), arXiv:hep-th/0304245 [hep-th].

[44] Boris Kors and Pran Nath, "Aspects of the Stueckelberg extension," JHEP **07**, 069 (2005), arXiv:hep-ph/0503208 [hep-ph].

[45] Kunal Kumar, Roberto Vega-Morales, and Felix Yu, "Effects from New Colored States and the Higgs Portal on Gluon Fusion and Higgs Decays," Phys. Rev. **D86**, 113002 (2012), [Erratum: Phys. Rev.D87,no.11,119903(2013)], arXiv:1205.4244 [hep-ph].

[46] David Tucker-Smith and Neal Weiner, "Inelastic dark matter," Phys. Rev. **D64**, 043502 (2001), arXiv:hep-ph/0101138 [hep-ph].

[47] Paolo Gondolo and Graciela Gelmini, "Cosmic abundances of stable particles: Improved analysis," Nucl. Phys. **B360**, 145–179 (1991).

[48] Jennifer A. Adams, Subir Sarkar, and D.W. Sciama, "CMB anisotropy in the decaying neutrino cosmology," Mon.Not.Roy.Astron.Soc. **301**, 210–214 (1998), arXiv:astro-ph/9805108 [astro-ph].

[49] Nikhil Padmanabhan and Douglas P. Finkbeiner, "Detecting Dark Matter Annihilation with CMB Polarization : Signatures and Experimental Prospects," Phys. Rev. **D72**, 023508 (2005), astro-ph/0503486.

[50] Silvia Galli, Fabio Iocco, Gianfranco Bertone, and Alessandro Melchiorri, "CMB constraints on Dark Matter models with large annihilation cross-section," Phys. Rev. **D80**, 023505 (2009), arXiv:0905.0003 [astro-ph.CO].

[51] Tracy R. Slatyer, Nikhil Padmanabhan, and Douglas P. Finkbeiner, "CMB Constraints on WIMP Annihilation: Energy Absorption During the Recombination Epoch," Phys. Rev. **D80**, 043526 (2009), arXiv:0906.1197 [astro-ph.CO].

[52] Douglas P. Finkbeiner, Silvia Galli, Tongyan Lin, and Tracy R. Slatyer, "Searching for Dark Matter in the CMB: A Compact Parameterization of Energy Injection from New Physics," Phys. Rev. **D85**, 043522 (2012), arXiv:1109.6322 [astro-ph.CO].

[53] Mathew S. Madhavacheril, Neelima Sehgal, and Tracy R. Slatyer, "Current Dark Matter Annihilation Constraints from Cmb and Low-Redshift Data," Phys. Rev. **D89**, 103508 (2014), arXiv:1310.3815 [astro-ph.CO].

[54] Julio F. Navarro, Carlos S. Frenk, and Simon D. M. White, "The Structure of cold dark matter halos," Astrophys. J. **462**, 563–575 (1996), arXiv:astro-ph/9508025 [astro-ph].

[55] Gilly Elor, Nicholas L. Rodd, Tracy R. Slatyer, and Wei Xue, "Model-Independent Indirect Detection Constraints on Hidden Sector Dark Matter," JCAP **1606**, 024 (2016), arXiv:1511.08787 [hep-ph].

[56] Lian-Bao Jia, "Study of WIMP annihilations into a pair of on-shell scalar mediators," Phys. Rev. **D94**, 095028 (2016), arXiv:1607.00737 [hep-ph].

[57] J. Alcaraz *et al.* (DELPHI, OPAL, ALEPH, LEP Electroweak Working Group, L3), "A Combination of preliminary electroweak measurements and constraints on the standard model," (2006), arXiv:hep-ex/0612034 [hep-ex].

[58] Georges Aad *et al.* (ATLAS), "Observation of a new particle in the search for the Standard Model Higgs boson with the ATLAS detector at the LHC," Phys. Lett. **B716**, 1–29 (2012), arXiv:1207.7214 [hep-ex].

[59] Serguei Chatrchyan *et al.* (CMS), "Observation of a new boson at a mass of 125 GeV with the CMS experiment at the LHC," Phys. Lett. **B716**, 30–61 (2012), arXiv:1207.7235 [hep-ex].

[60] Georges Aad *et al.* (ATLAS), "Constraints on new phenomena via Higgs boson couplings and invisible decays with the ATLAS detector," JHEP **11**, 206 (2015), arXiv:1509.00672 [hep-ex].

[61] Vardan Khachatryan *et al.* (CMS), "Searches for invisible decays of the Higgs boson in pp collisions at sqrt(s) = 7, 8, and 13 TeV," JHEP **02**, 135 (2017), arXiv:1610.09218 [hep-ex].

[62] Joachim Kopp, Jia Liu, Tracy R. Slatyer, Xiao-Ping Wang, and Wei Xue, "Impeded Dark Matter," JHEP **12**, 033 (2016), arXiv:1609.02147 [hep-ph].

[63] Adam Martin and Tuhin S. Roy, "The Gold-Plated Channel for Supersymmetric Higgs via Higgsphilic Z'," (2011), arXiv:1103.3504 [hep-ph].

[64] David Curtin *et al.*, "Exotic decays of the 125 GeV Higgs boson," Phys. Rev. **D90**, 075004 (2014), arXiv:1312.4992 [hep-ph].

[65] Jinrui Huang, Tao Liu, Lian-Tao Wang, and Felix Yu, "Supersymmetric Exotic Decays of the 125 GeV Higgs Boson," Phys. Rev. Lett. **112**, 221803 (2014), arXiv:1309.6633 [hep-ph].

[66] Jinrui Huang, Tao Liu, Lian-Tao Wang, and Felix Yu, "Supersymmetric subelectroweak scale dark matter, the Galactic Center gamma-ray excess, and exotic decays of the 125 GeV Higgs boson," Phys. Rev. **D90**, 115006 (2014), arXiv:1407.0038 [hep-ph].

[67] CMS Collaboration (CMS), "Search for a non-standard-model Higgs boson decaying to a pair of new light bosons in four-muon final states," (2013).

[68] "Properties of the Higgs-like boson in the decay H to ZZ to 4l in pp collisions at sqrt s =7 and 8 TeV," (2013).

[69] Georges Aad *et al.* (ATLAS), "Search for high-mass dilepton resonances in pp collisions at $\sqrt{s} = 8$ TeV with the ATLAS detector," Phys. Rev. **D90**, 052005 (2014), arXiv:1405.4123 [hep-ex].

[70] Vardan Khachatryan *et al.* (CMS), "Search for physics beyond the standard model in dilepton mass spectra in proton-proton collisions at $\sqrt{s} = 8$ TeV," JHEP **04**, 025 (2015), arXiv:1412.6302 [hep-ex].

[71] James M. Cline, Grace Dupuis, Zuowei Liu, and Wei Xue, "The windows for kinetically mixed Z'-mediated dark matter and the galactic center gamma ray excess," JHEP **08**, 131 (2014), arXiv:1405.7691 [hep-ph].

[72] Isaac Hoenig, Gabriel Samach, and David Tucker-Smith, "Searching for dilepton resonances below the Z mass at the LHC," Phys. Rev. **D90**, 075016 (2014), arXiv:1408.1075 [hep-ph].

[73] Serguei Chatrchyan *et al.* (CMS), "Measurement of the differential and double-differential Drell-Yan cross sections in proton-proton collisions at $\sqrt{s} = 7$ TeV," JHEP **12**, 030 (2013), arXiv:1310.7291 [hep-ex].

[74] Morad Aaboud *et al.* (ATLAS), "Search for high-mass new phenomena in the dilepton final state using proton-proton collisions at $\sqrt{s} = 13$ TeV with the ATLAS detector," Phys. Lett. **B761**, 372–392 (2016), arXiv:1607.03669 [hep-ex].

[75] Zhi-Cheng Liu, Chong-Xing Yue, and Yu-Chen Guo, "Single production of dark photon at the LHC," (2017), arXiv:1703.00153 [hep-ph].

[76] Georges Aad *et al.* (ATLAS), "Search for new phenomena in final states with an energetic jet and large missing transverse momentum in pp collisions at $\sqrt{s}$ =8 TeV with the ATLAS detector," Eur. Phys. J. **C75**, 299 (2015), [Erratum: Eur. Phys. J.C75,no.9,408(2015)], arXiv:1502.01518 [hep-ex].

[77] Vardan Khachatryan *et al.* (CMS), "Search for dark matter, extra dimensions, and unparticles in monojet events in proton–proton collisions at $\sqrt{s} = 8$ TeV," Eur. Phys. J. **C75**, 235 (2015), arXiv:1408.3583 [hep-ex].

[78] Thomas Jacques and Karl Nordstrom, "Mapping monojet constraints onto Simplified Dark Matter Models," JHEP **06**, 142 (2015), arXiv:1502.05721 [hep-ph].

[79] Mikael Chala, Felix Kahlhoefer, Matthew McCullough, Germano Nardini, and Kai Schmidt-Hoberg, "Constraining Dark Sectors with Monojets and Dijets," JHEP **07**, 089 (2015), arXiv:1503.05916 [hep-ph].

[80] A. J. Brennan, M. F. McDonald, J. Gramling, and T. D. Jacques, "Collide and Conquer: Constraints on Simplified Dark Matter Models using Mono-X Collider Searches," JHEP **05**, 112 (2016), arXiv:1603.01366 [hep-ph].

[81] Arpit Gupta, Reinard Primulando, and Prashant Saraswat, "A New Probe of Dark Sector Dynamics at the LHC," JHEP **09**, 079 (2015), arXiv:1504.01385 [hep-ph].

[82] Malte Buschmann, Joachim Kopp, Jia Liu, and Pedro A. N. Machado, "Lepton Jets from Radiating Dark Matter," JHEP **07**, 045 (2015), arXiv:1505.07459 [hep-ph].

[83] Mogens Dam, "Precision Electroweak measurements at the FCC-ee," (2016), arXiv:1601.03849 [hep-ex].

[84] David d'Enterria, "Physics at the FCC-ee," in *17th Lomonosov Conference on Elementary Particle Physics Moscow, Russia, August 20-26, 2015* (2016) arXiv:1602.05043 [hep-ex].

[85] Manqi Ruan, "Higgs Measurement at e^+e^- Circular Colliders," *Proceedings, 37th International Conference on High Energy Physics (ICHEP 2014): Valencia, Spain, July 2-9, 2014*, Nucl. Part. Phys. Proc. **273-275**, 857–862 (2016), arXiv:1411.5606 [hep-ex].

[86] J. Alwall, R. Frederix, S. Frixione, V. Hirschi, F. Maltoni, O. Mattelaer, H. S. Shao, T. Stelzer, P. Torrielli, and M. Zaro, "The automated computation of tree-level and next-to-leading order differential cross sections, and their matching to parton shower simulations," JHEP **07**, 079 (2014), arXiv:1405.0301 [hep-ph].

[87] Torbjorn Sjostrand, Stephen Mrenna, and Peter Z. Skands, "PYTHIA 6.4 Physics and Manual," JHEP **05**, 026 (2006), arXiv:hep-ph/0603175 [hep-ph].

[88] J. de Favereau, C. Delaere, P. Demin, A. Giammanco, V. Lemaître, A. Mertens, and M. Selvaggi (DELPHES 3), "DELPHES 3, A modular framework for fast simulation of a generic collider experiment," JHEP **02**, 057 (2014), arXiv:1307.6346 [hep-ex].

[89] Manqi Ruan (CEPC-SPPC study group), "https://indico.cern.ch/event/550509/contributions/2413240/attachments/139 [https://github.com/delphes/delphes/blob/master/cards/delphes_card_CEPC.tcl].

[90] C. Patrignani *et al.* (Particle Data Group), "Review of Particle Physics," Chin. Phys. **C40**, 100001 (2016).